Effects of geometric and material nonlinearities on tunable band gaps and low-frequency directionality of phononic crystals

Pai Wang,[1] Jongmin Shim,[2] and Katia Bertoldi[1,3]
[1]*School of Engineering and Applied Sciences, Harvard University, Cambridge, Massachusetts 02138, USA*
[2]*Department of Civil, Structural and Environmental Engineering, University at Buffalo, Buffalo, New York 14260, USA*
[3]*Kavli Institute, Harvard University, Cambridge, Massachusetts 02138, USA*
(Received 4 March 2013; published 22 July 2013)

We investigate the effects of geometric and material nonlinearities introduced by deformation on the linear dynamic response of two-dimensional phononic crystals. Our analysis not only shows that deformation can be effectively used to tune the band gaps and the directionality of the propagating waves, but also reveals how geometric and material nonlinearities contribute to the tunable response of phononic crystals. Our numerical study provides a better understanding of the tunable response of phononic crystals and opens avenues for the design of systems with optimized properties and enhanced tunability.

DOI: 10.1103/PhysRevB.88.014304 PACS number(s): 63.20.dd, 43.35.+d, 62.30.+d

Phononic crystals (i.e., periodic structures composed of multiple materials with contrast in mechanical properties) have attracted considerable interest due to their ability to tailor the propagation of waves through band gaps, frequency ranges in which the propagation of sound and elastic waves is forbidden.[1–5] This fundamental property has been recently exploited to design waveguides,[6] frequency modulators,[7] noise-reduction devices,[8] and vibration isolators.[9] It has also been recognized that phononic crystals are characterized by directional behavior that can be exploited to steer or redirect waves in specific directions.[3,10,11] The directionality is determined by the level of anisotropy of the structure and can be fully controlled through proper arrangement of the material distribution at the unit cell level.[12] Furthermore, many previous studies have focused on the high frequency propagation directionality of phononic crystals,[13–15] while the strongly directional behavior in the low frequency/long wavelength regime is not fully explored despite important potential applications in broadband situations.[12]

Motivated by technological applications, a number of studies investigated the effects of both material properties (i.e., contrast in density, Young's modulus, and Poisson's ratio)[16,17] and geometry (i.e., volume fraction and topology)[18,19] on the characteristics of phononic crystals. However, in all these investigations the band gaps and the directionality of the propagating waves are limited to specific values that cannot be tuned after the manufacturing process. New strategies are required to design phononic crystals with adaptive properties that can be reversibly tuned.

It has been recently demonstrated that mechanical loading can be used as a robust mechanism for *in situ* tunability of soft and highly deformable two-dimensional phononic crystals.[5] It was shown that both the position and width of the band gap are strongly affected by the applied deformation.[5,20,21] However, the effect of deformation on the directionality of the propagating waves in the low frequency regime (i.e., the first longitudinal and shear modes) has never been studied. Finally, although it is evident that the applied deformation induces both strong geometric and material nonlinearities,[5] it is not clear how these two factors contribute to the tunability of the response. To shed light on these important points, here we investigate not only the effect of the applied deformation on the low frequency directionality of the propagating waves, but also the contributions of geometric and material nonlinearities to the tunable response of soft phononic crystals. The numerical analyses performed in this study offer a better understanding of the tunable response of phononic crystals and provide guidelines for the design of structures with optimized properties and enhanced tunability.

Here we focus on two-dimensional (2D) soft phononic crystals. Although our analysis is general and can be applied to any architecture, in this study we present numerical results for a square array of circular holes characterized by an initial void volume fraction $V_0 = 60\%$ [Fig. 1(a)]. Here V_0 is defined as the volume of the voids divided by the total volume of the phononic crystal. The nonlinear finite-element code ABAQUS/STANDARD is used to deform the structures as well as to investigate the propagation of small-amplitude elastic waves in the predeformed phononic crystal. Detailed description of the general formulation and the numerical simulations are provided in the Supplementary Materials.[22]

For all the analyses, 2D finite element models are constructed and the accuracy of the mesh is ascertained through a mesh refinement study. We focus on a phononic crystal made of an almost-incompressible elastomeric material whose response is captured by a Gent model[23] characterized by the following strain energy density function:

$$W(I_1, J) = -\frac{G}{2} J_m \log\left(\frac{J_m - (I_1 - 3)}{J_m}\right) - G\log(J) + \left(\frac{K}{2} - \frac{G}{J_m}\right)(J-1)^2, \quad (1)$$

where $I_1 = \mathrm{trace}(\mathbf{F}^T\mathbf{F})$, $J = \det(\mathbf{F})$, $\mathbf{F}$ denotes the deformation gradient, G and K are the initial shear and bulk moduli, and J_m denotes a material constant related to the strain at saturation. We note that the strain energy tends to infinity as $I_1 - 3$ approaches J_m.

Here we consider an elastomeric material with $G = 1.08 \times 10^6$ N/m^2, $K = 2.0 \times 10^9$ N/m^2 (Poisson's ratio $\nu = 0.4997$), and $\rho_0 = 1050$ kg/m^3, so that in the undeformed configuration the elastic wave speeds for shear and

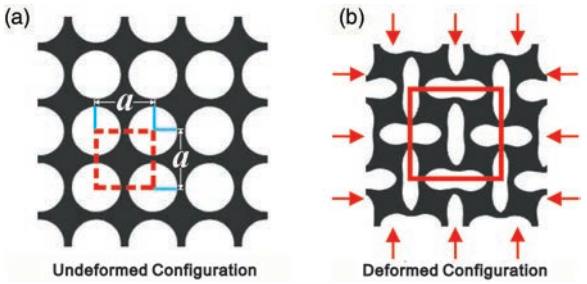

FIG. 1. (Color online) Geometry reorganization induced by instability in a soft phononic crystal comprising a square array of circular holes subjected to equibiaxial compression. The dashed square of size $a \times a$ in (a) indicates the primitive unit cell in the undeformed configuration. The solid square in (b) represents the enlarged representative volume element in the deformed configuration.

pressure waves in the material are $c_T = 32.07$ m/s and $c_L = 1381$ m/s, respectively. The effects of material nonlinearities are investigated by considering three different values of J_m, $J_m = 0.5, 2.0, \infty$. Note that, at the limit of $J_m \to \infty$, the strain energy density function (1) reduces to that of a Neo-Hookean material.[22,24] In Fig. 2 the material response under uniaxial loading is reported in terms of the nominal stress S, normalized by G, versus the uniaxial deformation stretch. The results clearly indicate that smaller values of J_m introduce stronger nonlinearities in the material behavior.

It is well known that, under compression, the geometric pattern of soft phononic crystals can suddenly change due to either: (a) microscopic instabilities with a spatial periodicity comparable to the size of the unit cell; or (b) macroscopic instabilities with a spatial periodicity much larger than the size of the unit cell.[25–28] Note that a detailed description of both micro- and macroscopic instabilities and the numerical procedure to calculate the onset of each case is provided in the Supplementary Materials.[22] In this study we investigate both instabilities of the phononic crystal under equibiaxial

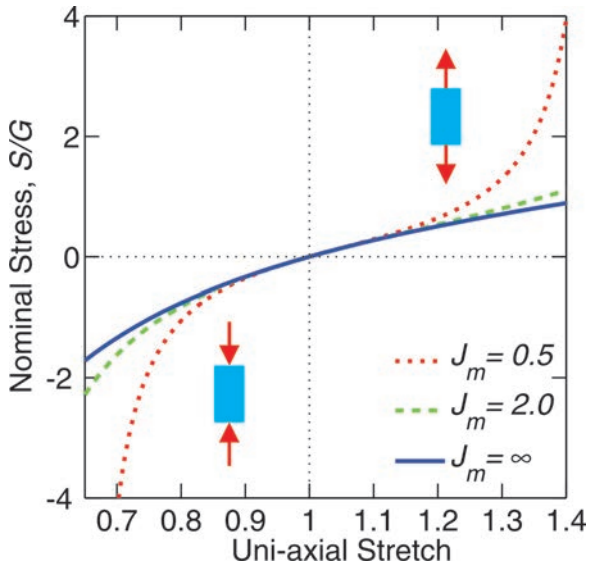

FIG. 2. (Color online) Uniaxial stress-stretch response of a nearly incompressible Gent material with $J_m = 0.5$, 2.0, and ∞ (the last corresponding to a Neo-Hookean material).

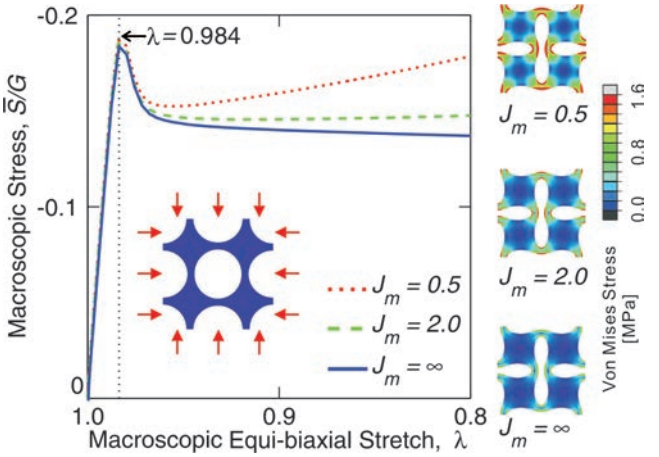

FIG. 3. (Color online) Macroscopic nominal stress vs stretch curves for the square array of circular holes in a Gent matrix. The departure from linearity is the result of an elastic instability that triggers the pattern transformation. The Von Mises stress distributions in the phononic crystals at $\lambda = 0.8$ are shown on the right for $J_m = 0.5$, 2.0, and ∞.

compression, so that the macroscopic deformation gradient $\bar{\mathbf{F}}$ is given by

$$\bar{\mathbf{F}} = \lambda(\mathbf{e}_1 \otimes \mathbf{e}_1 + \mathbf{e}_2 \otimes \mathbf{e}_2), \tag{2}$$

where λ denotes the macroscopically applied stretch and $\mathbf{e}_1$ and $\mathbf{e}_1$ are the basis vectors of two-dimensional Cartesian coordinates. We note that the undeformed configuration is characterized by $\lambda = 1$. Moreover, $\lambda > 1$ and $\lambda < 1$ represent the tension and compression load, respectively.

For the considered periodic structure, the onsets of both microscopic and macroscopic instabilities are detected by studying the response of a single unit cell [indicated by the dashed red square in Fig. 1(a)] along the loading path (2) by decreasing λ from unity. For all the cases considered here (i.e., $J_m = 0.5, 2.0, \infty$), a microscopic instability is detected at $\lambda_{\text{cr}}^{\text{Micro}} = 0.984$, while the onset of macroscopic instability occurs at $\lambda_{\text{cr}}^{\text{Macro}} = 0.961$. Therefore, microscopic instabilities are always critical in compression, leading to an enlarged representative volume element of 2×2 primitive unit cells and to the formation of a pattern of alternating, mutually orthogonal and elongated holes [Fig. 1(b)].

The postbuckling response of the phononic crystal is then simulated by introducing small random imperfections in the initial geometry.[22] In Fig. 3 we present the static response of the phononic crystal for the three considered values of J_m in terms of the macroscopically effective nominal stress $\bar{S}$ versus the applied stretch λ. Although the onset of instability is found not to be affected by J_m, we can clearly see that J_m has a strong influence on the postbuckling response of the structure.

To highlight the effect of the applied deformation on the propagation of elastic waves, we present in Fig. 4 the band structure and directionality diagrams of a phononic crystal made of a Gent material with $J_m = 0.5$ in both the undeformed [$\lambda = 1.0$, Fig. 4(a)] and deformed [$\lambda = 0.8$, Fig. 4(b)] configurations.

Figures 4(c) and 4(d) show the band diagrams of the undeformed and deformed configurations, respectively. The

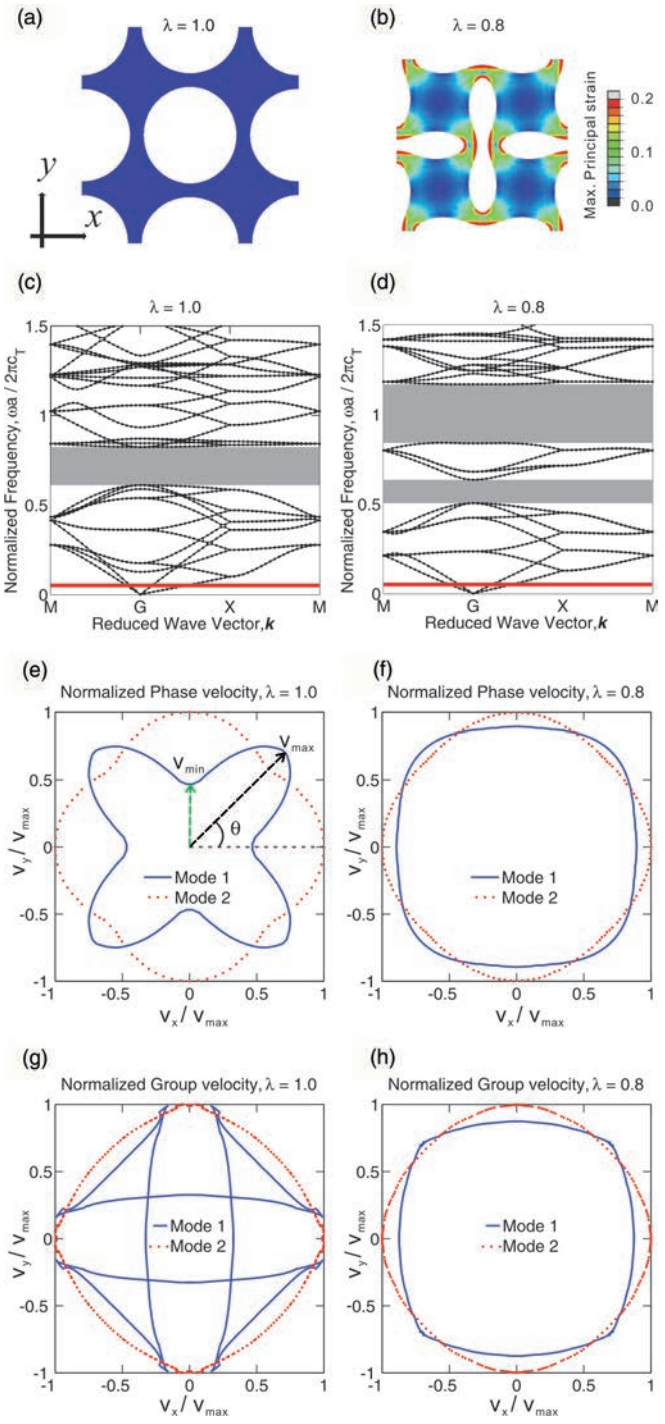

FIG. 4. (Color online) Dynamic response of the phononic crystal in the undeformed (left column, $\lambda = 1.0$) and deformed (right column, $\lambda = 0.8$) configuration. (c) and (d): effect of deformation on the band gaps. (e) and (f): effect of deformation on the directionality of phase velocities. (g) and (h): effect of deformation on the directionality of group velocities.

dimensionless frequency $\tilde{f} = \omega a/(2\pi c_T)$, with a denoting the characteristic size of the unit cell in the undeformed configuration [Fig. 1(a)], is plotted as a function of the wave vector in the reciprocal space.[22] In the undeformed configuration, the periodic structure features a band gap at $\tilde{f} = 0.61$–0.82. It is clear from Fig. 4(d) that the compression significantly alters the band structure. The pre-existing band gap is shifted and widened to $\tilde{f} = 0.84$–1.29. In addition, a new band gap that does not exist in the reference state is opened at $\tilde{f} = 0.50$–0.64.

To investigate the effect of deformation on the preferential directions of wave propagation, we focus on the low frequency range and calculate both phase velocity and group velocity for all directions of propagation at $\tilde{f} = 0.05$ [horizontal red line in Figs. 4(c) and 4(d)].[22] In Figs. 4(e) and 4(f) we report the phase velocity profiles and in Figs. 4(g) and 4(h) the group velocity profiles for the undeformed and deformed configurations, respectively. In these plots all the wave velocities are normalized, so that the magnitude of maximum velocity $v_{\max}$ of any mode in any configuration is unity. It is important to note that the wave directionality in the low frequency range cannot be fully captured just by inspecting the band diagrams.[12] In fact, although the dispersion curves at low frequency resemble straight lines, which seem to imply linear dispersion relations, the approximation of an effective nondispersive media is not applicable here, as phase and group velocities may exhibit very different directional behaviors.[12]

We start by noting that, in the undeformed configuration, the phase velocity shows a preferred direction of propagation at $\theta = 45^\circ$ for mode 1 (shear-dominated mode) and at $\theta = 0^\circ$ for mode 2 (pressure-dominated mode) [Fig. 4(e)]. Moreover, the group velocity in the undeformed configuration exhibits two preferred directions at $\theta = 10^\circ$ and 80° for mode 1 [Fig. 4(g)], whereas it does not show a significant preferential direction of propagation for mode 2. Finally, we note that the loped pattern in Fig. 4(g) entails two different group velocities in certain directions [a feature that cannot be directly observed in the standard dispersion relation in Fig. 4(c)]. In general, the group velocity, which is defined as the gradient of the dispersion surface,[22] can be at a different direction than the direction of the wave vector. Hence, two wave vectors of different directions may result in two group velocities of different magnitudes in the same direction.

In contrast, the deformed configuration does not exhibit any strong preference in directions for both phase and group velocities in both modes [Figs. 4(f) and 4(h)], so that it behaves as a nearly isotropic medium. These results clearly indicate that the deformation has a significant effect on the wave's directionality. Finally, we observe that the applied deformation has a more pronounced effect on the phase and group velocity profiles of mode 1 (shear-dominated mode), whereas the directionality of mode 2 (pressure-dominated mode) is only marginally affected.

The results presented above clearly show that the applied deformation strongly affects not only the static, but also the dynamic response of phononic crystals. However, to design the next generation of tunable phononic crystals that take full advantage of the changes on the dynamic response induced by the applied deformation, this mechanism needs to be thoroughly understood. While it is well known that the applied deformation introduces both geometric and material nonlinearities, it is not clear how these two effects control the tunable dynamic response of the phononic crystal. To gain knowledge on this front, we numerically investigate the separate effects of geometric and material nonlinearities on both the band gaps and wave directionality.

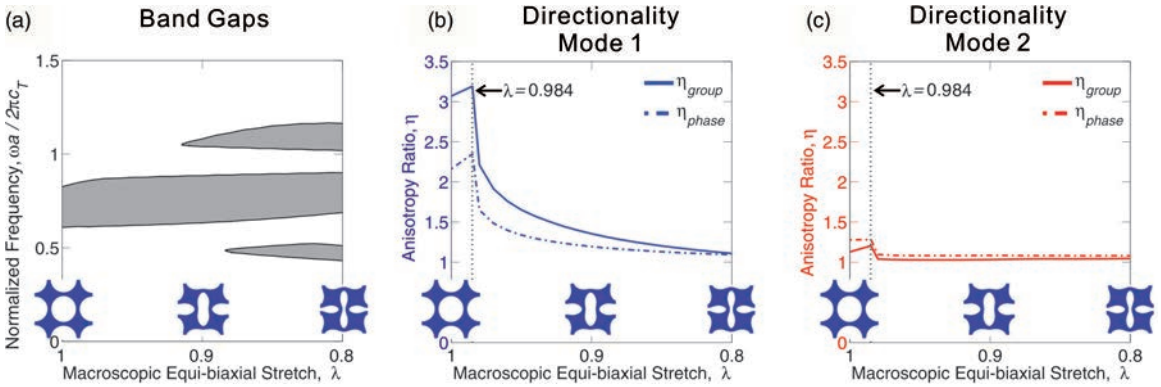

FIG. 5. (Color online) Effects of geometric nonlinearities on (a) band gaps and directionality of (b) mode 1 and (c) mode 2.

Geometric nonlinearities. To evaluate the effect of geometric nonlinearities on the dynamic response of the phononic crystal, we investigate the propagation of elastic waves in a stress-free structure with the deformed geometry (i.e., the shape of the structure is determined by the postbuckling analysis). More specifically, we compress the structure up to a certain value of λ and then set the all the components of the stress to zero before performing the wave propagation analysis. Thus, the inhomogeneous stress distribution is not taken into the consideration when computing the dynamic response.

The evolution of the band gaps as a function of λ is shown in Fig. 5(a). The change in geometry induced by the applied deformation is found to shift and widen the main band gap and to generate two additional band gaps, one higher and the other lower than the main gap, which open at $\lambda = 0.92$ and $\lambda = 0.88$, respectively. These deformation-induced band gaps also shift and widen for decreasing values of λ. Finally, we note that these results are independent of J_m since in order to investigate the geometric effects alone, we have neglected the stress distribution in the deformed configuration (note that the incremental response for an unstressed Gent material is independent of J_m).

To describe the evolution of the directionality of propagating waves, we define the anisotropy ratio:

$$\eta = \frac{v_{\max}}{v_{\min}}, \tag{3}$$

where $v_{\max}$ and $v_{\min}$ are the maximum and minimum wave velocities, respectively [see Fig. 4(e)]. The trends of η for both phase velocity and group velocity of mode 1 (shear-dominated mode) and mode 2 (pressure-dominated mode) as a function of λ are reported in Figs. 5(b) and 5(c), respectively.

For mode 1, the anisotropy ratios of both the group and phase velocity profiles (η_{group} and η_{phase}) rise from the initial values up to a turning point, then rapidly decrease as a function of λ and approach unity [Fig. 5(b)]. Note that the turning point at $\lambda = 0.984$ corresponds to the onset of structural instability. Similar trends are observed for mode 2 [Fig. 5(c)], but the changes induced by deformation are less dramatic in this case. In summary, the results from both modes show that the geometric nonlinearities induced by instability have a significant effect on the wave directionality. They remove the directional characteristics of both modes and make the wave propagation more isotropic.

Material nonlinearities. It is apparent from Fig. 4(b) that deformation not only affects the geometry, but also induces an inhomogeneous strain/stress distribution within the phononic crystal. Substantial stress concentrations are developed during compression and they strongly depend on the nonlinear material response, which is characterized by J_m (Fig. 3).

To investigate the effect of material nonlinearities on the propagation of elastic waves, we start by studying the response of a phononic crystal made of a Neo-Hookean material (i.e., Gent material with $J_m = \infty$). The response of such material is weakly nonlinear and the stiffening effect induced by the applied deformation is negligible in this case. In Fig. 6(a) we report the evolution of the band gaps as a function of the

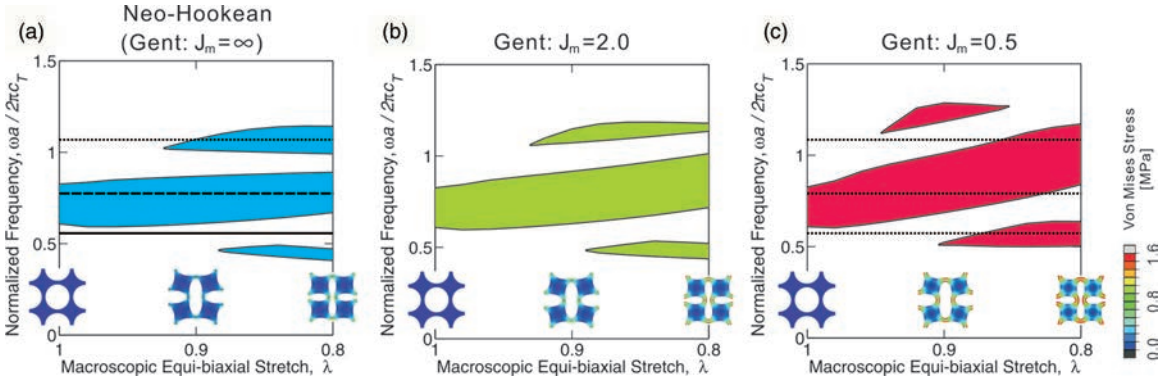

FIG. 6. (Color online) Effects of material nonlinearities on the band gaps. Soft phononic crystals made of Gent materials with (a) $J_m = \infty$, (b) $J_m = 2.0$, and (c) $J_m = 0.5$ are investigated.

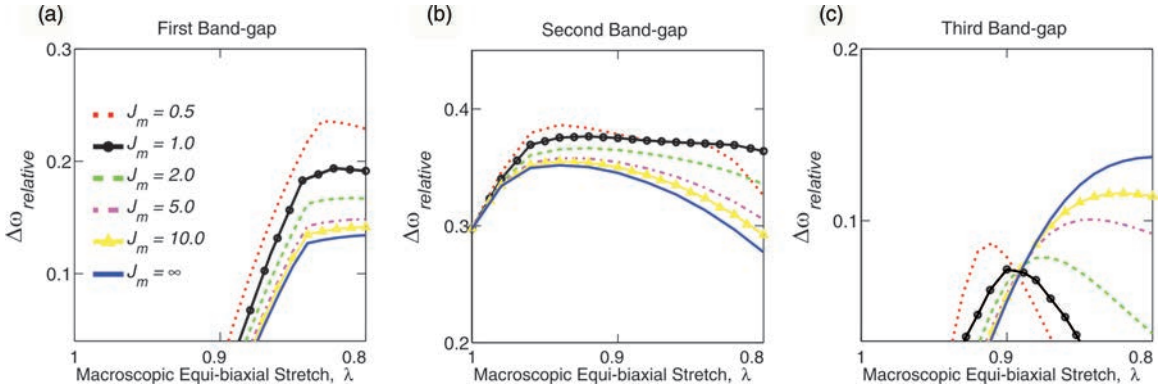

FIG. 7. (Color online) Comparison of the change of relative band gaps during deformation.

applied deformation λ. Comparison between Figs. 5(a) and 6(a) reveals that the dynamic response of the phononic crystal is not affected by the inhomogeneous stress state. Therefore, for a phononic crystal made of an Neo-Hookean elastomeric material, the geometric nonlinearities induced by the applied deformation fully control the position and width of the band gaps.

Next, we investigate the evolution of the band gaps for phononic crystals made of elastomers with stronger material nonlinearity. As shown in Fig. 2, smaller values of J_m introduce stronger material nonlinearities under the applied deformation. Here we comparatively study the cases of phononic crystals made of Gent materials with $J_m = 2.0$ and 0.5 [Figs. 6(b) and 6(c)]. We notice that in both cases the band gaps are significantly affected by material nonlinearities when $\lambda < 0.9$. We find that smaller values of J_m provide a larger range of tunability for the band gaps. To better quantify the effect of material nonlinearity on the band gap tunability, we divide the wave frequencies into three categories: (i) frequencies that are always in the propagating band [e.g., $\tilde{f} = 0.55$, continuous horizontal line in Fig. 6(a)]; (ii) frequencies that are always in the band gap [e.g., $\tilde{f} = 0.75$, dashed horizontal line in Fig. 6(a)]; and (iii) frequencies that can be switched on/off by the applied deformation [e.g., $\tilde{f} = 1.05$, dotted horizontal line in Fig. 6(a)]. We start by noting that all the three frequencies highlighted in Fig. 6(a) turn into category (iii) when $J_m = 0.5$ [see dotted horizontal lines in Fig. 6(c)]. In fact, for $J_m = 0.5$, the frequencies in the entire region $\tilde{f} =$ 0.49–1.28 can be switched on/off by the applied deformation. Therefore, since large regions of type (iii) frequencies are desirable for the design of a highly tunable system, our results indicate that phononic crystals made of materials with stronger nonlinearities can offer enhanced band gap tunability.

In addition, our analysis also reveals that material nonlinearities do not affect the directionality of the propagating waves at low frequency. The velocity profiles obtained for phononic crystals made of Gent material with $J_m = \infty$, 2.0, and 0.5 are found to be the same as those shown in Figs. 5(b) and 5(c). The same behavior is also observed for the case of triangular and trihexagonal arrays of circular holes (see Supplementary Materials),[22] suggesting that only changes in geometry can be effectively used to tune the directional characteristics of the lower bands. This is due to the fact that the wavelength of the low frequency propagating modes are very long compared with the length scale of the local variations of stress field.

To further study the effect of the material parameter J_m on the band gaps, we calculate the relative size of the band gaps as the ratio between gap width and the midgap position,

$$\Delta\omega_{\text{relative}} = \frac{\omega_{\text{upper}} - \omega_{\text{lower}}}{(\omega_{\text{upper}} + \omega_{\text{lower}})/2}, \tag{4}$$

where ω_{upper} and ω_{lower} are the frequencies of upper and lower edge limits of a band gap, respectively. It has been previously shown that the relative size defined above is a important design parameter, and that a large relative size of the band gap is preferable for many applications.[4] The evolution of $\Delta\omega_{\text{relative}}$ as a function of the applied deformation is reported in Figs. 7(a)–7(c) for the first, second, and third band gap, respectively. The responses of phononic crystals made of Gent material with $J_m = 0.5$, 1.0, 2.0, 5.0, 10.0, and ∞ are considered. For all different materials considered here and for all three band gaps $\Delta\omega_{\text{relative}}$ is found first to increase as a function of the applied deformation, then to reach a maximum and finally either to plateau or slightly decrease. For instance, in the case of $J_m = 0.5$, $\Delta\omega_{\text{relative}}$ reaches the maximum value at $\lambda = 0.83$, 0.94, and 0.91 for the first, second, and third band gaps, respectively. We note that the decrease of $\Delta\omega_{\text{relative}}$ after its maximum is due to the fact that the position shifting effect is stronger than the widening effect. That is, in Eq. (4), the increase in the denominator becomes faster than the increase in the numerator. As a result, although the band gap keeps widening upon further deformation, $\Delta\omega_{\text{relative}}$ diminishes. This feature described above becomes more pronounced when the applied deformation is large and the constituting material is highly nonlinear.

To summarize, we use numerical simulations to study the propagation of small-amplitude elastic waves in highly deformed phononic crystals and investigate the effect of deformation on band gaps and directionality of propagating waves. The contributions of geometric and material nonlinearities to the tunable response of phononic crystals are revealed. The band gaps are found to be affected both by geometric and material nonlinearities, while the directional preferences of the wave modes in the first two bands are shown to be sensitive only to changes in geometry. Enhanced tunability of the band gaps is found for phononic crystals made of materials with

stronger nonlinear behavior. Finally, the changes in geometry introduced by the applied deformation gradually remove the directional characteristics of the lowest two propagation modes, making the wave propagation more isotropic. The results presented in this paper provide useful guidelines for the design of tunable phononic devices.

This work has been supported by Harvard MRSEC through Grant No. DMR-0820484 and by NSF through Grants No. CMMI-1120724 and No. CMMI-1149456 (CAREER). K.B. acknowledges start-up funds from the Harvard School of Engineering and Applied Sciences and the support of the Kavli Institute and Wyss Institute at Harvard University.

[1]M. Sigalas and E. Economou, Solid State Commun. **86**, 141 (1993).
[2]M. S. Kushwaha, P. Halevi, L. Dobrzynski, and B. Djafari-Rouhani, Phys. Rev. Lett. **71**, 2022 (1993).
[3]M. Ruzzene and F. Scarpa, Phys. Status Solidi B **242**, 665 (2005).
[4]M. Maldovan and E. Thomas, Appl. Phys. B **83**, 595 (2006).
[5]K. Bertoldi and M. C. Boyce, Phys. Rev. B **78**, 184107 (2008).
[6]J. O. Vasseur, A. Hennion, B. Rouhani, F. Duval, B. Dubus, and Y. Pennec, J. App. Phys. **101**, 114904 (2007).
[7]W. Cheng, J. J. Wang, U. Jonas, G. Fytas, and N. Stefanou, Nat. Mater. **5**, 830 (2006).
[8]F. Casadei, L. Dozio, M. Ruzzene, and K. Cunefare, J. Sound. Vib. **329**, 3632 (2010).
[9]F. Casadei, B. Beck, K. A. Cunefare, and M. Ruzzene, J. Intel. Mat. Syst. Str. **23**, 1169 (2012).
[10]M. Ruzzene, F. Scarpa, and F. Soranna, Smart. Mater. Struct. **12**, 363 (2003).
[11]M. Collet, M. Ouisse, M. Ruzzene, and M. N. Ichchou, Int. J. Solids Struct. **48**, 2837 (2011).
[12]F. Casadei and J. J. Rimoli, Int. J. Solids Struct. **50**, 1402 (2013).
[13]E. Nolde, R. Craster, and J. Kaplunov, J. Mech. Phys. Solids **59**, 651 (2011).
[14]S. Gonella and M. Ruzzene, Int. J. Solids Struct. **45**, 2897 (2008).
[15]S. Gonella and M. Ruzzene, J. Sound Vib. **312**, 125 (2008).
[16]J. O. Vasseur, B. Djafari-Rouhani, L. Dobrzynski, M. S. Kushwaha, and P. Halevi, J. Phys. Condens. Mater. **6**, 8759 (1994).
[17]X. Zhou, Y. Wang, and C. Zhang, J. Appl. Phys. **106**, 014903 (2009).
[18]A. B. Movchan, N. V. Movchan, and S. Haq, Mater. Sci. Eng. **431**, 175 (2006).
[19]M. Maldovan and E. Thomas, *Periodic Materials and Interference Lithography for Photonics, Phononics and Mechanics* (Wiley-VCH, Berlin, 2009).
[20]J. Jang, C. Koh, K. Bertoldi, M. Boyce, and E. Thomas, Nano Lett. **9**, 2113 (2009).
[21]L. Wang and K. Bertoldi, Int. J. Solids Struct. **49**, 2881 (2012).
[22]See Supplemental Material at http://link.aps.org/supplemental/10.1103/PhysRevB.88.014304 for the details of the general formulation and numerical procedures.
[23]A. Gent, Rubber Chem. Tech. **69**, 59 (1996).
[24]L. Treloar, Trans. Faraday Soc. **40**, 59 (1944).
[25]G. Geymonat, S. Muller, and N. Triantafyllidis, Arch. Ration. Mech. Anal. **122**, 231 (1993).
[26]N. Triantafyllidis, M. D. Nestorovic, and M. W. Schraad, J. Appl. Mech. **73**, 505 (2006).
[27]K. Bertoldi, M. Boyce, S. Deschanel, S. M. Prange, and T. Mullin., J. Mech. Phys. Solids **56**, 2642 (2008).
[28]Overvelde, S. Shan, and K. Bertoldi, Adv. Mater. **24**, 2337 (2012).

Supplementary Materials for Effects of Geometric and Material Non-linearities on the Tunable Response of Phononic Crystals

Pai Wang,[1] Jongmin Shim,[2] and Katia Bertoldi[1,3]

[1]School of Engineering and Applied Sciences, Harvard University, Cambridge, Massachusetts 02138, USA
[2]Department of Civil, Structural and Environmental Engineering, Buffalo, New York 14260, USA
[3]Kavli Institute, Harvard University, Cambridge, Massachusetts 02138, USA

(Dated: July 22, 2013)

PACS numbers: 63.20.dd 43.35.+d 62.30.+d

GENERAL FORMULATION

Here, we present fundamental relations (i.e., governing equations, boundary conditions and material models) which are employed in the manuscript.

Governing Equations

We consider two-dimensional (2D) infinitely periodic solids and assume plane strain conditions. Their deformation is described by the deformation gradient

$$\mathbf{F} = \frac{\partial \mathbf{x}}{\partial \mathbf{x}_0}, \tag{1}$$

mapping a point in the material from the reference position $\mathbf{x}_0$ to its current location $\mathbf{x}$. The material is assumed to be non-linear elastic, characterized by a stored-energy function $W = W(\mathbf{F})$, which is defined in the reference configuration. The first Piola-Kirchhoff stress $\mathbf{S}$ is thus related to the deformation gradient $\mathbf{F}$ by

$$\mathbf{S} = \frac{\partial W}{\partial \mathbf{F}}. \tag{2}$$

In the absence of body forces, the equation of motions in the reference configuration can be written as

$$\mathrm{Div}\,\mathbf{S} = \rho_0 \frac{D^2\mathbf{x}}{Dt^2}, \tag{3}$$

where Div represents the divergence operator in the undeformed/reference configuration, D/Dt is the material time derivative and ρ_0 denotes the reference mass density.

To investigate the effect of the applied deformation on the propagation of small-amplitude elastic waves, incremental deformations superimposed upon a given state of finite deformation are considered. Denoting with $\dot{\mathbf{S}}$ the increment of the first Piola-Kirchhoff stress, the incremental forms of the governing equations is given by

$$\mathrm{Div}\,\dot{\mathbf{S}} = \rho_0 \frac{D^2\dot{\mathbf{x}}}{Dt^2}, \tag{4}$$

where $\dot{\mathbf{x}}$ denotes the incremental displacements. Furthermore, linearization of the constitutive equation (2) yields

$$\dot{\mathbf{S}} = \mathbb{L} : \dot{\mathbf{F}}, \;\; \text{with} \;\; \mathbb{L}_{ijkl} = \frac{\partial^2 W}{\partial F_{ij} \partial F_{kl}}, \tag{5}$$

where $\dot{\mathbf{F}}$ denotes the the incremental deformation gradient.

The incremental boundary value problem is often formulated in an updated Lagrangian formulation, where the deformed state is used as the reference configuration for the calculation of the incremental quantities [1]. Push-forward transformations allow the introduction of the incremental updated stress quantity $\boldsymbol{\Sigma}$ given by

$$\boldsymbol{\Sigma} = \frac{1}{J}\dot{\mathbf{S}}\mathbf{F}^T. \tag{6}$$

For a non-linear elastic material, the incremental constitutive equation takes the linear form

$$\boldsymbol{\Sigma} = \mathbb{C} : \mathrm{grad}\,\mathbf{u}, \tag{7}$$

to the first order, where grad denotes the gradient operator in the deformed/current configuration, $\mathbf{u} \doteq \dot{\mathbf{x}}$ and

$$\mathbb{C}_{ijkl} = J^{-1} F_{jn} F_{lq} \frac{\partial^2 W}{\partial F_{in} \partial F_{kq}}. \tag{8}$$

Finally, the incremental equations of motions take the form

$$\mathrm{div}\boldsymbol{\Sigma} = \rho \frac{d^2\mathbf{u}}{dt^2}, \tag{9}$$

where div represents the divergence operator in the deformed/current configuration, ρ denotes the current material density and d/dt is the spatial time derivative.

Here, we focus on the propagation of small-amplitude elastic waves defined by

$$\mathbf{u}(\mathbf{x}, t) = \widetilde{\mathbf{u}}(\mathbf{x}) \exp(-i\omega t)\ , \tag{10}$$

where ω is the angular frequency of the propagating wave, and $\widetilde{\mathbf{u}}$ denotes the magnitude of the incremental displacement. It follows from (7) that

$$\boldsymbol{\Sigma}(\mathbf{x}, t) = \widetilde{\boldsymbol{\Sigma}}(\mathbf{x}) \exp(-i\omega t)\ , \tag{11}$$

so that equations (9) become

$$\mathrm{div}\widetilde{\mathbf{\Sigma}} = \rho\,\omega^2\widetilde{\mathbf{u}}\ , \tag{12}$$

which represent the frequency-domain wave equations.

Infinite Periodic Structures

Here we focus on 2D periodic solid of infinite extent characterized by a primitive cell (i.e. minimum unit identified in the periodic structure), which is specified by the lattice vectors $\mathbf{a}_1$ and $\mathbf{a}_2$, as shown in Fig. 1A. Thus, any spatial function field, $\phi(\mathbf{x})$, in the infinite periodic structure satisfies the condition:

$$\phi(\mathbf{x}+\mathbf{p}) = \phi(\mathbf{x}), \tag{13}$$

where

$$\mathbf{p} = p_1\mathbf{a}_1 + p_2\mathbf{a}_2, \tag{14}$$

where p_1 and p_2 are arbitrary integers.

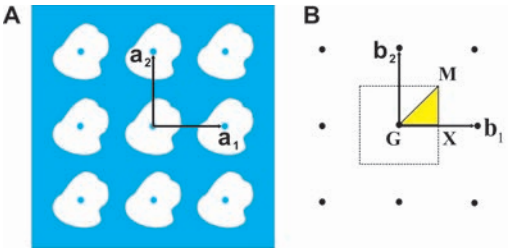

FIG. 1: Point Lattice (blue dots in A), reciprocal lattice (black dots in B), first Brillioun zone (square area in B) and irreducible Brillioun zone (IBZ, Triangle **GXM** in B).

For later use, we define the reciprocal lattice specified by the reciprocal lattice vectors $\mathbf{b}_1$ and $\mathbf{b}_2$ defined such that

$$\mathbf{a}_i \cdot \mathbf{b}_j = 2\pi\delta_{ij}, \tag{15}$$

where δ_{ij} is the Kronecker delta. It follows that $\mathbf{b}_1$ and $\mathbf{b}_2$ are defined as

$$\mathbf{b}_1 = 2\pi\frac{\mathbf{a}_2\times\mathbf{z}}{\parallel\mathbf{z}\parallel^2}\ , \quad \mathbf{b}_2 = 2\pi\frac{\mathbf{z}\times\mathbf{a}_1}{\parallel\mathbf{z}\parallel^2}\ , \tag{16}$$

where $\mathbf{z} = \mathbf{a}_1\times\mathbf{a}_2$. As shown in Fig. 1B, the reciprocal lattice is characterized by spatial periodicity $\mathbf{g}$

$$\mathbf{g} = g_1\mathbf{b}_1 + g_2\mathbf{b}_2, \tag{17}$$

with g_1 and g_2 being arbitrary integers. Therefore, any function $\psi(\mathbf{k})$ defined in the reciprocal space satisfies the condition

$$\psi(\mathbf{k}+\mathbf{g}) = \psi(\mathbf{k}). \tag{18}$$

Next, in the reciprocal space we identify the *first Brillioun zone* (area inside the square in Fig. 1B) [2], defined by the reciprocal lattice points. For the analysis of waves propagating in periodic structures, it has been shown that only wave vectors in first Brillioun zone need to be considered. In addition, we may further reduce the domain taking advantage of its reflectional and rotational symmetries. The reduced domain is referred as the *irreducible Brillioun zone (IBZ)* (triangle **GXM** in Fig. 1B) [3].

Material Models

Here we focus on isotropic, nearly incompressible and hyper-elastic rubber-like materials. Both the Gent [4] and the Neo-Hookean [5] models are considered to investigate the effect of material non-linearity on wave propagation.

Gent Model

The compressible version of the strain energy function proposed by Gent [4] is given by

$$\begin{aligned} W(I_1,J) = &-\frac{G}{2}J_m\log\left(1-\frac{I_1-3}{J_m}\right) - G\log(J) \\ &+\left(\frac{K}{2}-\frac{G}{J_m}\right)(J-1)^2, \end{aligned} \tag{19}$$

where $I_1 = \mathrm{trace}\left(\mathbf{F}^T\mathbf{F}\right)$, $J = \det(\mathbf{F})$, G and K are the initial shear and bulk moduli, and J_m denotes a material constant related to the strain at saturation, since since the stress become infinite as $J_m - I_1 + 3$ approaches zero.

Substituting (19) into (2) and (5), the nominal stress $\mathbf{S}$ and the incremental modulus $\mathbb{L}$ are obtained as

$$\mathbf{S} = \frac{GJ_m}{J_m-I_1+3}\mathbf{F} + \left[\left(K-\frac{2G}{J_m}\right)J(J-1) - G\right]\mathbf{F}^{-T}, \tag{20}$$

and

$$\begin{aligned} \mathbb{L} = &\frac{GJ_m}{J_m-I_1+3}\mathbb{I} + \frac{2GJ_m}{(J_m-I_1+3)^2}\mathbf{F}\otimes\mathbf{F} \\ &+ J(2J-1)\left(K-\frac{2G}{J_m}\right)\mathbf{F}^{-T}\otimes\mathbf{F}^{-T} \\ &+ \left[J(J-1)\left(K-\frac{2G}{J_m}\right) - G\right]\mathbb{A}, \end{aligned} \tag{21}$$

where

$$\mathbb{I}_{ijkl} = \frac{\partial F_{kl}}{\partial F_{ij}} = \delta_{ik}\delta_{jl}, \tag{22}$$

and

$$\mathbb{A}_{ijkl} = \frac{\partial F_{kl}^{-T}}{\partial F_{ij}} = -F_{il}^{-T} F_{kj}^{-T}. \tag{23}$$

In Fig. 2 we report the material response for an almost incompressible material with $K/G = 2000$. Uniaxial loading conditions are considered, so that

$$\mathbf{F} = \lambda \mathbf{e}_1 \otimes \mathbf{e}_1 + \tilde{\lambda} \mathbf{e}_2 \otimes \mathbf{e}_2 + \mathbf{e}_3 \otimes \mathbf{e}_3, \tag{24}$$

λ denoting the applied stretch and $\tilde{\lambda}$ being such that $S_{22} = 0$. In Fig. 2 the material response in terms of the dimensionless nominal stress S_{11}/G versus applied stretch λ is reported for three different values of J_m. The results clearly indicate that small values of J_m introduce strong non-linearities.

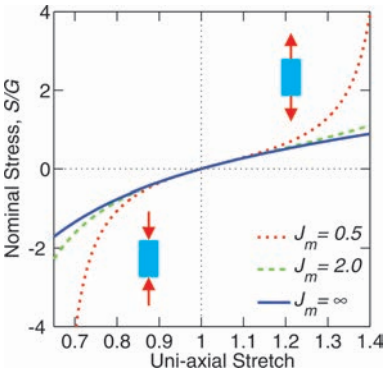

FIG. 2: Uniaxial stress-stretch response of a nearly incompressible Gent material with $J_m = 0.5$, 2.0 and ∞ (the last corresponding to a Neo-Hookean material).

Neo-Hookean Model

We note that as $J_m \to +\infty$ the Gent model reduces to the Neo-Hookean model [5], for which the compressible version of the strain energy density function is given by

$$W(I_1, J) = \frac{G}{2}(I_1 - 3) - G\log(J) + \frac{K}{2}(J-1)^2 \ , \tag{25}$$

It also follows that $\mathbf{S}$ and $\mathbb{L}$ for a Neo-Hookean material are given by

$$\mathbf{S} = G\mathbf{F} + [KJ(J-1) - G]\,\mathbf{F}^{-T}, \tag{26}$$

and

$$\begin{aligned}\mathbb{L} = {} & G\mathbb{I} + KJ(2J-1)\mathbf{F}^{-T} \otimes \mathbf{F}^{-T} \\ & + [KJ(J-1) - G]\,\mathbb{I}^T.\end{aligned} \tag{27}$$

NUMERICAL PROCEDURE AND IMPLEMENTATION

The finite element framework is used to deform the structures as well as to investigate the propagation of elastic waves at different level of applied deformation. Each simulation consists of the following three steps: A) buckling analysis, B) post-buckling analysis, and C) wave propagation analysis. In this Section we provide a detailed description of the numerical analysis performed in these three steps.

Buckling Analysis

As the first step in the numerical simulation, the buckling analysis is performed on a primitive unit cell. The structural integrity of periodic structures under applied deformation is a critical issue which is frequently overlooked. In fact, when periodic porous structures are deformed their spatial periodicity can suddenly change due to mechanical instability and it is useful to make the distinction between *microscopic* instabilities (i.e. instabilities with wavelengths that are of the order of the size of the microstructure) and *macroscopic* instabilities (i.e. instabilities with much larger wavelengths comparable to the size of the unit cell) [6–9].

Microscopic Instabilities

Although microscopic (local) buckling modes may alter the initial periodicity of the solid, they can be still detected by studying the response of a single unit cell and investigating the propagation of small-amplitude waves with arbitrary wave vector $\check{\mathbf{k}}$ superimposed on the current state of deformation [6–8]. While a real angular frequency ω corresponds to a propagating wave, a complex ω identifies a perturbation exponentially growing with time. Therefore, the transition between a stable and an unstable configuration is detected when the frequency vanishes (i.e. $\omega = 0$) and the new periodicity of the solid introduced by instability can be easily obtained by the corresponding wave vector.

To detect the onset of microscopic instabilities, we first deform the primitive unit cell to a certain extent and then investigate the propagation of elastic waves with different wave vector

$$\check{\mathbf{k}} = \check{k}_1 \mathbf{b}_1 + \check{k}_2 \mathbf{b}_2, \tag{28}$$

$\check{k}_1$ and $\check{k}_2$ being two real numbers. For each wave vector $\check{\mathbf{k}}$, the angular frequency ω is determined by solving the frequency domain equation (12). In this analysis quasi-periodic boundary conditions are applied, so that

$$\mathbf{u}(\mathbf{x} + \check{\mathbf{r}}) = \mathbf{u}(\mathbf{x}) \exp(i\check{\mathbf{k}} \cdot \check{\mathbf{r}}), \tag{29}$$

$\check{\mathbf{r}}$ denoting the distance in the current configuration between each pair of nodes periodically located on the boundary. Since most commercial finite-element packages do not support the complex-valued displacements

introduced by (29), following Aberg and Gudmundson [10] we split any complex-valued spatial function $\phi(\mathbf{x})$ into a real and an imaginary part,

$$\phi(\mathbf{x}) = \phi(\mathbf{x})^{re} + i\phi(\mathbf{x})^{im}. \tag{30}$$

The problem is then solved using two identical finite-element meshes for the unit cell, one for the real part and the other for the imaginary part, coupled by

$$\mathbf{u}^{re}(\mathbf{x}+\check{\mathbf{r}}) = \mathbf{u}^{re}(\mathbf{x})\cos(\check{\mathbf{k}}\cdot\check{\mathbf{r}}) - \mathbf{u}^{im}(\mathbf{x})\sin(\check{\mathbf{k}}\cdot\check{\mathbf{r}}), \tag{31}$$

$$\mathbf{u}^{im}(\mathbf{x}+\check{\mathbf{r}}) = \mathbf{u}^{re}(\mathbf{x})\sin(\check{\mathbf{k}}\cdot\check{\mathbf{r}}) + \mathbf{u}^{im}(\mathbf{x})\cos(\check{\mathbf{k}}\cdot\check{\mathbf{r}}). \tag{32}$$

A microscopic instability is detected at the first point along the loading path for which a wave vector $\check{\mathbf{k}}_{cr} = \check{k}_{1,cr}\mathbf{b}_1 + \check{k}_{2,cr}\mathbf{b}_2$ exist such that the corresponding angular frequency ω is zero. The instability will result in an enlarged unit cell with $n_1 \times n_2$ primitive unit cells, where

$$n_1 = \frac{1}{\check{k}_{1,cr}}, \quad \text{and} \quad n_2 = \frac{1}{\check{k}_{2,cr}}. \tag{33}$$

Macroscopic Instabilities

Following Geymonat et al. [6], we examine macroscopic instabilities by detecting loss of strong ellipticity of the overall response of the periodic structure. Specifically, macroscopic instabilities may develop whenever the condition

$$(\mathbf{m}\otimes\mathbf{M}) : \left[\mathbb{L}^H : (\mathbf{m}\otimes\mathbf{M})\right] > 0\ , \quad \text{for all} \quad \mathbf{m}\otimes\mathbf{M} \neq \mathbf{0} \tag{34}$$

is first violated along the loading path, $\mathbb{L}^H$ denoting the homogenized incremental modulus.

Operationally, after determining the principal solution, the components of $\mathbb{L}^H$ are identified by subjecting the unit cells to four independent linear perturbations of the macroscopic deformation gradient [8]. Then loss of ellipticity is examined by checking condition (34) at every $\pi/360$ radian increment.

Post-buckling Analysis

As the second step, the post-buckling analysis is performed to capture the response of the structure beyond instability. Models with $n_1 \times n_2$ primitive unit cells are built, where n_1 and n_2 are determined in the buckling analysis. We first introduce a small random imperfection in the initial geometry by perturbing the position of each node. Here, we use a uniform random perturbation on each node with amplitude equal to one percent of the smallest element edge in the mesh.

Periodic boundary conditions are then applied, so that the positions of each pair of nodes periodically located on the boundary satisfy

$$\mathbf{x}(\mathbf{x}_0 + \mathbf{r_0}) - \mathbf{x}(\mathbf{x}_0) = \overline{\mathbf{F}}\cdot\mathbf{r_0} \tag{35}$$

where $\bar{\mathbf{F}}$ denotes the macroscopic deformation gradient and $\mathbf{r_0}$ the distance in the undeformed configuration between each pair of periodically located nodes.

Wave Propagation Analysis

In order to obtain the dispersion relation and evaluate the directionality of the propagating waves for the phononic crystals, frequency domain wave propagation analysis are performed on the deformed configurations generated by the post-buckling analysis. Bloch-type boundary conditions (eqns. (31) and (32)) are applied with the propagating bloch-wave vector $\mathbf{k}$ and updated spatial periodicity $\mathbf{r}$, so that

$$\mathbf{u}^{re}(\mathbf{x}+\mathbf{r}) = \mathbf{u}^{re}(\mathbf{x})\cos(\mathbf{k}\cdot\mathbf{r}) - \mathbf{u}^{im}(\mathbf{x})\sin(\mathbf{k}\cdot\mathbf{r}), \tag{36}$$

$$\mathbf{u}^{im}(\mathbf{x}+\mathbf{r}) = \mathbf{u}^{re}(\mathbf{x})\sin(\mathbf{k}\cdot\mathbf{r}) + \mathbf{u}^{im}(\mathbf{x})\cos(\mathbf{k}\cdot\mathbf{r}). \tag{37}$$

Focusing on the propagation of small-amplitude waves, we solve eqn. (12) using a perturbation method to obtain the dispersion relations $\omega = \omega(\mathbf{k})$.

For a 2D infinite periodic structure with spatial periodicity defined by (13) and (14), the periodicity in the reciprocal $\mathbf{k}$-space of the dispersion relation is given by [2]:

$$\omega(\mathbf{k}+\mathbf{g}) = \omega(\mathbf{k}), \tag{38}$$

with $\mathbf{g}$ defined in (17). Hence, due to translational symmetry specified by (38), we only need to study $\omega(\mathbf{k})$ for $\mathbf{k}$ vectors in the *first Brillouin zone* [2]. Moreover, the domain can be further reduced by taking advantage of rotational, reflectional and inversional symmetries of the first Brillouin zone. This allows us to define the *irreducible Brillouin zone* (IBZ) (see yellow triangle in Fig. 1) [3].

The phononic bandgaps are identified by checking all eigen-frequencies $\omega(\mathbf{k})$ for $\mathbf{k}$ vectors on the perimeter of the IBZ. The bandgaps (i.e. range in frequencies for which the propagation of waves is barred) are given by the frequency ranges within which no $\omega(\mathbf{k})$ exist. Numerically, a discrete set of $\mathbf{k}$ vectors on the IBZ perimeter need to be chosen in the band-gap calculation. For the simulations presented in this paper, twenty uniformly spaced points on each edge of the IBZ are used for the purpose of identifying band-gaps.

For the propagation directionality of the elastic wave in passing band of the phononic crystal, we investigate

the eigen-frequency surfaces over the entire IBZ to get the iso-frequency plots of the first two modes of the lowest passing bands: mode 1 being a shear-dominated mode and mode 2 representing a pressure-dominated mode. The phase velocity $\mathbf{v}_p$ and group velocity $\mathbf{v}_g$ of the propagating wave are then calculated as

$$\mathbf{v}_p = \frac{\omega \mathbf{k}}{\| \mathbf{k} \|^2} \ , \quad \mathbf{v}_g = \frac{\partial \omega}{\partial \mathbf{k}}. \tag{39}$$

Numerically, a discrete set of $\mathbf{k}$ vectors in the IBZ need to be chosen in the analysis. For the simulations presented in this paper, the results from four hundred uniformly distributed points inside the IBZ are used to interpolate the dispersion surface in $k-$space. Then, the value of dimensionless frequency $\tilde{f} = \omega a/(2\pi c_T) = 0.05$ is fixed for the calculation of the wave velocities of the low frequency modes (the first and second modes). Lastly, a standard central difference scheme is adopted for the calculation of the group velocity.

ADDITIONAL RESULTS FOR LOW-FREQUENCY DIRECTIONALITY

The results included in the main text suggest that *material nonlinearity* only affects the band gap and does not affect the propagation direction at low frequencies. Although in the main text we only include results for a square array of circular holes, we observed the same behavior also for different lattice patterns, non-linear material models and void volume fractions. Here, we report the results obtained not only for a square (Fig. 3), but also for triangular (Fig. 4) and trihexagonal (Fig. 5) arrays of circular holes with 60% initial porosity. The details and deformation configurations of these patterns can be found in [11]. In the figures, iso-frequency plots of the first shear-dominated (Mode 1) and pressure-dominated (Mode 2) modes are reported for the undeformed (top) and deformed (center and bottom) configurations. Moreover, for the deformed configurations both the Neo-Hookean model (i.e. Gent material with $J_m = \infty$, center) and the Gent model with $J_m = 0.5$ (bottom) are considered. It is important to note that for the deformed configurations the iso-frequency profiles obtained for phononic crystals made of Gent material with $J_m = \infty$ and 0.5 are found to be the same for all patterns. In contrast, we find a significant difference in the iso-frequency profiles between the undeformed and deformed configurations. These results suggest that only changes in geometry can be effectively used to tune the directional characteristics of the lowest two modes. This is due to the fact that the wavelength of the low frequency propagating modes are very long compared with the length scale of the local variations of stress field.

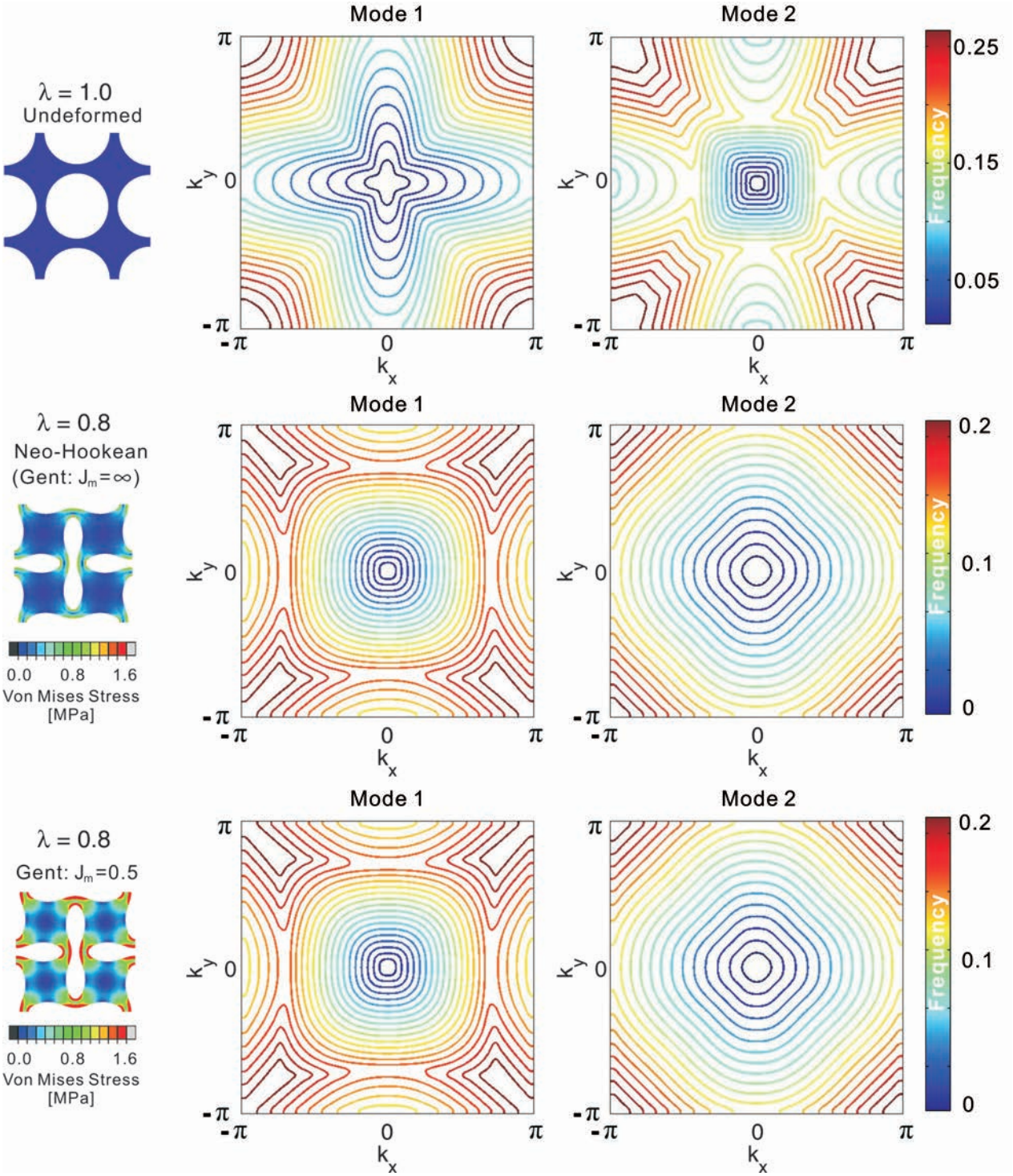

FIG. 3: Iso-frequency plots of the first two modes for the square lattice of circular voids. The results are reported in terms of the normalized frequency $\tilde{f} = \omega a/(2\pi c_T)$

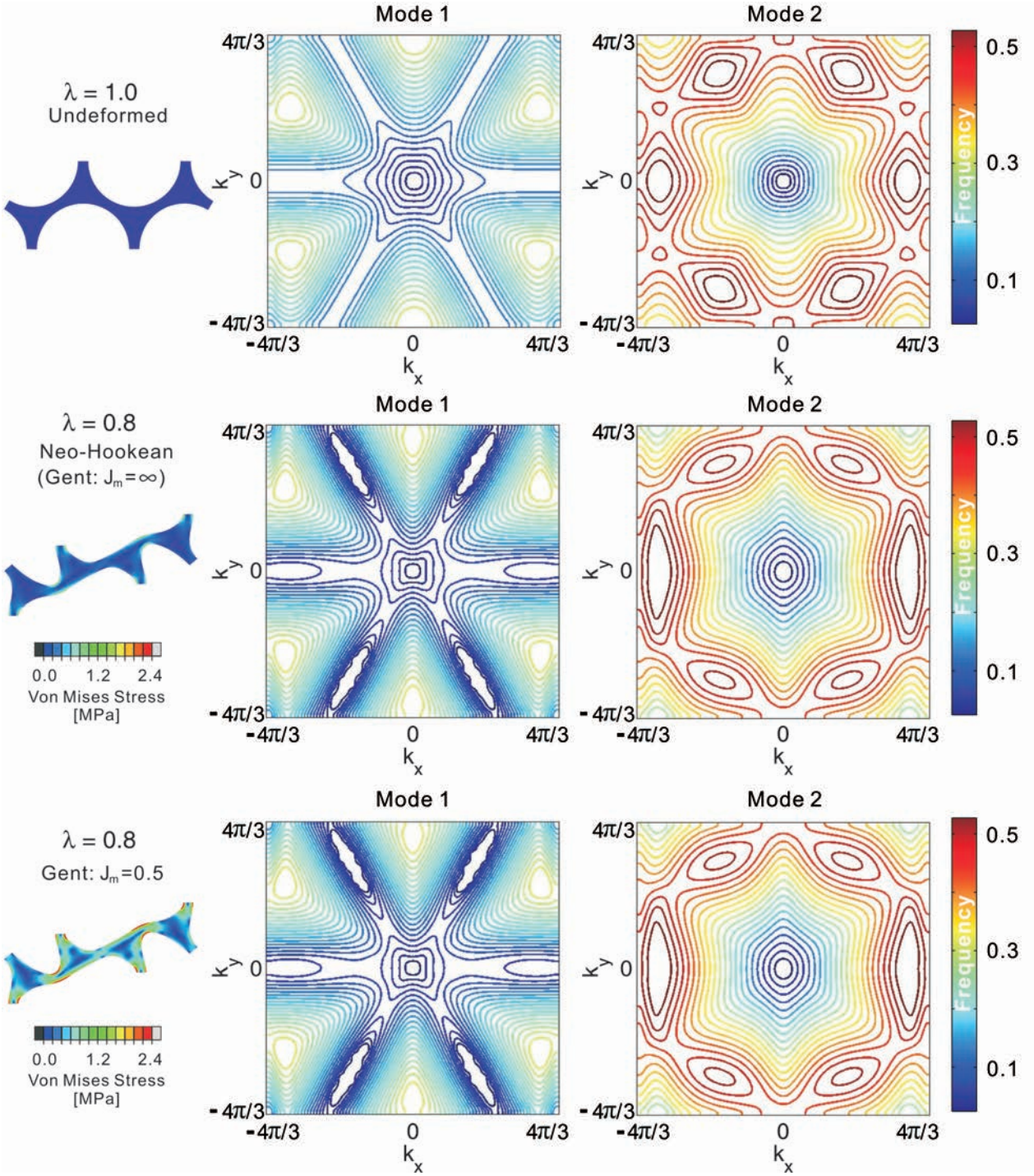

FIG. 4: Iso-frequency plots of the first two modes for the triangular lattice of circular voids. The results are reported in terms of the normalized frequency $\tilde{f} = \omega a/(2\pi c_T)$

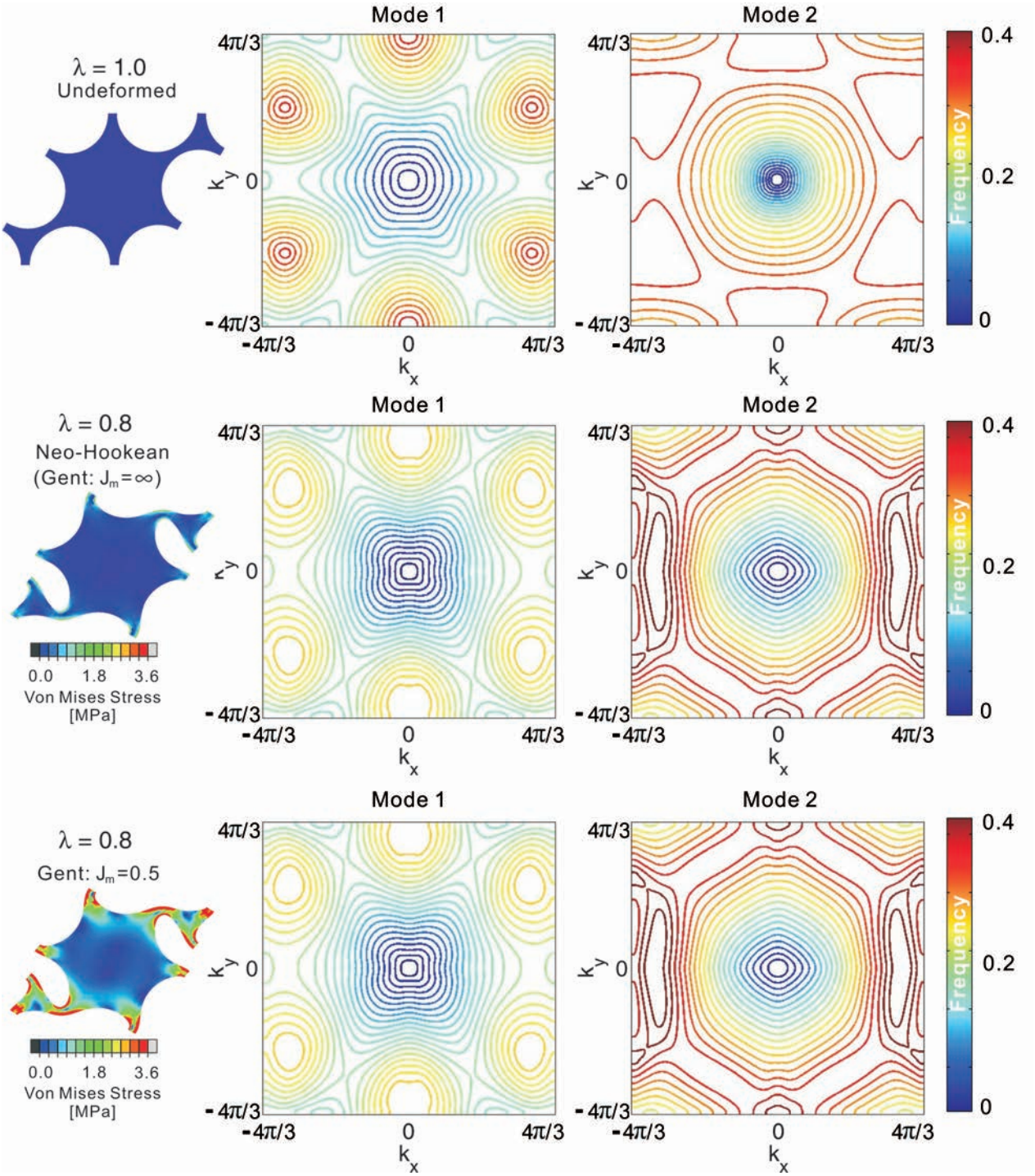

FIG. 5: Iso-frequency plots of the first two modes for the trihexagonal lattice of circular voids. The results are reported in terms of the normalized frequency $\tilde{f} = \omega a/(2\pi c_T)$

[1] R. W. Ogden, *Non-Linear Elastic Deformations* (Dover, 1997).
[2] L. Brillouin, *Wave Propagation in Periodic Structures* (McGraw-Hill, 1946).
[3] M. Maldovan and E. Thomas, *Periodic Materials and Interference Lithography for Photonics, Phononics and Mechanics* (Wiley-VCH, 2009).
[4] A. Gent, Rubber Chem. Tech. **69**, 59 (1996).
[5] L. Treloar, Trans. Faraday Soc. **40**, 59 (1944).
[6] G. Geymonat, S. Muller, and N. Triantafyllidis, Arch. Ration. Mech. Anal. **122**, 231 (1993).
[7] N. Triantafyllidis, M. D. Nestorovic, and M. W. Schraad, J. Appl. Mech. **73**, 505 (2006).
[8] K. Bertoldi, M. Boyce, S. Deschanel, S. M. Prange, and T. Mullin., J. Mech. Phys. Solids **56**, 2642 (2008).
[9] Overvelde, S. Shan, and K. Bertoldi, Adv. Mater. **24**, 2337 (2012).
[10] M. Aberg and P. Gudmundson, J. Acoust. Soc. Am. **102**, 2007 (1997).
[11] J. Shim, S. Shan, A. Kosmrlj, S. H. Kang, E. R. Chen, J. C. Weaver, and K. Bertoldi, Soft Matter (2013).

Supplementary Materials for Effects of Geometric and Material Non-linearities on the Tunable Response of Phononic Crystals

Pai Wang,[1] Jongmin Shim,[1] and Katia Bertoldi[1,2]

[1]School of Engineering and Applied Sciences, Harvard University, Cambridge, Massachusetts 02138, USA
[2]Kavli Institute, Harvard University, Cambridge, Massachusetts 02138, USA

(Dated: July 8, 2013)

PACS numbers: 63.20.dd 43.35.+d 62.30.+d

GENERAL FORMULATION

Here, we present fundamental relations (i.e., governing equations, boundary conditions and material models) which are employed in the manuscript.

Governing Equations

We consider two-dimensional (2D) infinitely periodic solids and assume plane strain conditions. Their deformation is described by the deformation gradient

$$\mathbf{F} = \frac{\partial \mathbf{x}}{\partial \mathbf{x}_0}, \tag{1}$$

mapping a point in the material from the reference position $\mathbf{x}_0$ to its current location $\mathbf{x}$. The material is assumed to be non-linear elastic, characterized by a stored-energy function $W = W(\mathbf{F})$, which is defined in the reference configuration. The first Piola-Kirchhoff stress $\mathbf{S}$ is thus related to the deformation gradient $\mathbf{F}$ by

$$\mathbf{S} = \frac{\partial W}{\partial \mathbf{F}}. \tag{2}$$

In the absence of body forces, the equation of motions in the reference configuration can be written as

$$\mathrm{Div}\,\mathbf{S} = \rho_0 \frac{D^2\mathbf{x}}{Dt^2}, \tag{3}$$

where Div represents the divergence operator in the undeformed/reference configuration, D/Dt is the material time derivative and ρ_0 denotes the reference mass density.

To investigate the effect of the applied deformation on the propagation of small-amplitude elastic waves, incremental deformations superimposed upon a given state of finite deformation are considered. Denoting with $\dot{\mathbf{S}}$ the increment of the first Piola-Kirchhoff stress, the incremental forms of the governing equations is given by

$$\mathrm{Div}\,\dot{\mathbf{S}} = \rho_0 \frac{D^2\dot{\mathbf{x}}}{Dt^2}, \tag{4}$$

where $\dot{\mathbf{x}}$ denotes the incremental displacements. Furthermore, linearization of the constitutive equation (2) yields

$$\dot{\mathbf{S}} = \mathbb{L} : \dot{\mathbf{F}}, \;\; \text{with} \;\; \mathbb{L}_{ijkl} = \frac{\partial^2 W}{\partial F_{ij} \partial F_{kl}}, \tag{5}$$

where $\dot{\mathbf{F}}$ denotes the the incremental deformation gradient.

The incremental boundary value problem is often formulated in an updated Lagrangian formulation, where the deformed state is used as the reference configuration for the calculation of the incremental quantities [**?**]. Push-forward transformations allow the introduction of the incremental updated stress quantity $\mathbf{\Sigma}$ given by

$$\mathbf{\Sigma} = \frac{1}{J}\dot{\mathbf{S}}\mathbf{F}^T. \tag{6}$$

For a non-linear elastic material, the incremental constitutive equation takes the linear form

$$\mathbf{\Sigma} = \mathbb{C} : \mathrm{grad}\,\mathbf{u}, \tag{7}$$

to the first order, where grad denotes the gradient operator in the deformed/current configuration, $\mathbf{u} \doteq \dot{\mathbf{x}}$ and

$$\mathbb{C}_{ijkl} = J^{-1} F_{jn} F_{lq} \frac{\partial^2 W}{\partial F_{in} \partial F_{kq}}. \tag{8}$$

Finally, the incremental equations of motions take the form

$$\mathrm{div}\mathbf{\Sigma} = \rho \frac{d^2\mathbf{u}}{dt^2}, \tag{9}$$

where div represents the divergence operator in the deformed/current configuration, ρ denotes the current material density and d/dt is the spatial time derivative.

Here, we focus on the propagation of small-amplitude elastic waves defined by

$$\mathbf{u}(\mathbf{x}, t) = \widetilde{\mathbf{u}}(\mathbf{x}) \exp(-i\omega t)\ , \tag{10}$$

where ω is the angular frequency of the propagating wave, and $\widetilde{\mathbf{u}}$ denotes the magnitude of the incremental displacement. It follows from (7) that

$$\mathbf{\Sigma}(\mathbf{x}, t) = \widetilde{\mathbf{\Sigma}}(\mathbf{x}) \exp(-i\omega t)\ , \tag{11}$$

so that equations (9) become

$$\mathrm{div}\widetilde{\mathbf{\Sigma}} = \rho\omega^2\widetilde{\mathbf{u}}\ , \tag{12}$$

which represent the frequency-domain wave equations.

Infinite Periodic Structures

Here we focus on 2D periodic solid of infinite extent characterized by a primitive cell (i.e. minimum unit identified in the periodic structure), which is specified by the lattice vectors $\mathbf{a}_1$ and $\mathbf{a}_2$, as shown in Fig. 1A. Thus, any spatial function field, $\phi(\mathbf{x})$, in the infinite periodic structure satisfies the condition:

$$\phi(\mathbf{x}+\mathbf{p}) = \phi(\mathbf{x}), \tag{13}$$

where

$$\mathbf{p} = p_1\mathbf{a}_1 + p_2\mathbf{a}_2, \tag{14}$$

where p_1 and p_2 are arbitrary integers.

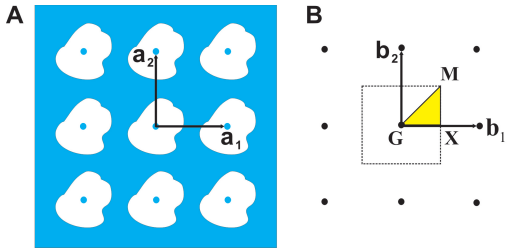

FIG. 1: Point Lattice (blue dots in A), reciprocal lattice (black dots in B), first Brillioun zone (square area in B) and irreducible Brillioun zone (IBZ, Triangle **GXM** in B).

For later use, we define the reciprocal lattice specified by the reciprocal lattice vectors $\mathbf{b}_1$ and $\mathbf{b}_2$ defined such that

$$\mathbf{a}_i \cdot \mathbf{b}_j = 2\pi\delta_{ij}, \tag{15}$$

where δ_{ij} is the Kronecker delta. It follows that $\mathbf{b}_1$ and $\mathbf{b}_2$ are defined as

$$\mathbf{b}_1 = 2\pi\frac{\mathbf{a}_2\times\mathbf{z}}{\parallel\mathbf{z}\parallel^2}\ , \quad \mathbf{b}_2 = 2\pi\frac{\mathbf{z}\times\mathbf{a}_1}{\parallel\mathbf{z}\parallel^2}\ , \tag{16}$$

where $\mathbf{z} = \mathbf{a}_1\times\mathbf{a}_2$. As shown in Fig. 1B, the reciprocal lattice is characterized by spatial periodicity $\mathbf{g}$

$$\mathbf{g} = g_1\mathbf{b}_1 + g_2\mathbf{b}_2, \tag{17}$$

with g_1 and g_2 being arbitrary integers. Therefore, any function $\psi(\mathbf{k})$ defined in the reciprocal space satisfies the condition

$$\psi(\mathbf{k}+\mathbf{g}) = \psi(\mathbf{k}). \tag{18}$$

Next, in the reciprocal space we identify the *first Brillioun zone* (area inside the square in Fig. 1B) [**?**], defined by the reciprocal lattice points. For the analysis of waves propagating in periodic structures, it has been shown that only wave vectors in first Brillioun zone need to be considered. In addition, we may further reduce the domain taking advantage of its reflectional and rotational symmetries. The reduced domain is referred as the *irreducible Brillioun zone (IBZ)* (triangle **GXM** in Fig. 1B) [19].

Material Models

Here we focus on isotropic, nearly incompressible and hyper-elastic rubber-like materials. Both the Gent [23] and the Neo-Hookean [24] models are considered to investigate the effect of material non-linearity on wave propagation.

Gent Model

The compressible version of the strain energy function proposed by Gent [23] is given by

$$W(I_1,J) = -\frac{G}{2}J_m\log\left(1-\frac{I_1-3}{J_m}\right) - G\log(J) + \left(\frac{K}{2}-\frac{G}{J_m}\right)(J-1)^2, \tag{19}$$

where $I_1 = \mathrm{trace}\left(\mathbf{F}^T\mathbf{F}\right)$, $J = \det(\mathbf{F})$, G and K are the initial shear and bulk moduli, and J_m denotes a material constant related to the strain at saturation, since since the stress become infinite as $J_m - I_1 + 3$ approaches zero.

Substituting (19) into (2) and (5), the nominal stress $\mathbf{S}$ and the incremental modulus $\mathbb{L}$ are obtained as

$$\mathbf{S} = \frac{GJ_m}{J_m-I_1+3}\mathbf{F} + \left[\left(K-\frac{2G}{J_m}\right)J(J-1)-G\right]\mathbf{F}^{-T}, \tag{20}$$

and

$$\begin{aligned}\mathbb{L} =& \frac{GJ_m}{J_m-I_1+3}\mathbb{I} + \frac{2GJ_m}{(J_m-I_1+3)^2}\mathbf{F}\otimes\mathbf{F} \\ &+ J(2J-1)\left(K-\frac{2G}{J_m}\right)\mathbf{F}^{-T}\otimes\mathbf{F}^{-T} \\ &+ \left[J(J-1)\left(K-\frac{2G}{J_m}\right)-G\right]\mathbb{A},\end{aligned} \tag{21}$$

where

$$\mathbb{I}_{ijkl} = \frac{\partial F_{kl}}{\partial F_{ij}} = \delta_{ik}\delta_{jl}, \tag{22}$$

and

$$\mathbb{A}_{ijkl} = \frac{\partial F^{-T}_{kl}}{\partial F_{ij}} = -F^{-T}_{il} F^{-T}_{kj}. \tag{23}$$

In Fig. 2 we report the material response for an almost incompressible material with $K/G = 2000$. Uniaxial loading conditions are considered, so that

$$\mathbf{F} = \lambda \mathbf{e}_1 \otimes \mathbf{e}_1 + \tilde{\lambda} \mathbf{e}_2 \otimes \mathbf{e}_2 + \mathbf{e}_3 \otimes \mathbf{e}_3, \tag{24}$$

λ denoting the applied stretch and $\tilde{\lambda}$ being such that $S_{22} = 0$. In Fig. 2 the material response in terms of the dimensionless nominal stress S_{11}/G versus applied stretch λ is reported for three different values of J_m. The results clearly indicate that small values of J_m introduce strong non-linearities.

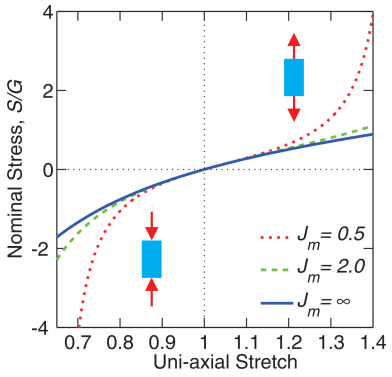

FIG. 2: Uniaxial stress-stretch response of a nearly incompressible Gent material with $J_m = 0.5$, 2.0 and ∞ (the last corresponding to a Neo-Hookean material).

Neo-Hookean Model

We note that as $J_m \to +\infty$ the Gent model reduces to the Neo-Hookean model [24], for which the compressible version of the strain energy density function is given by

$$W(I_1, J) = \frac{G}{2}(I_1 - 3) - G\log(J) + \frac{K}{2}(J-1)^2 \ , \tag{25}$$

It also follows that $\mathbf{S}$ and $\mathbb{L}$ for a Neo-Hookean material are given by

$$\mathbf{S} = G\mathbf{F} + [KJ(J-1) - G]\,\mathbf{F}^{-T}, \tag{26}$$

and

$$\begin{aligned}\mathbb{L} = G\mathbb{I} + KJ(2J-1)\mathbf{F}^{-T} \otimes \mathbf{F}^{-T} \\ + [KJ(J-1) - G]\,\mathbb{I}^T.\end{aligned} \tag{27}$$

NUMERICAL PROCEDURE AND IMPLEMENTATION

The finite element framework is used to deform the structures as well as to investigate the propagation of elastic waves at different level of applied deformation. Each simulation consists of the following three steps: A) buckling analysis, B) post-buckling analysis, and C) wave propagation analysis. In this Section we provide a detailed description of the numerical analysis performed in these three steps.

Buckling Analysis

As the first step in the numerical simulation, the buckling analysis is performed on a primitive unit cell. The structural integrity of periodic structures under applied deformation is a critical issue which is frequently overlooked. In fact, when periodic porous structures are deformed their spatial periodicity can suddenly change due to mechanical instability and it is useful to make the distinction between *microscopic* instabilities (i.e. instabilities with wavelengths that are of the order of the size of the microstructure) and *macroscopic* instabilities (i.e. instabilities with much larger wavelengths comparable to the size of the unit cell) [25–28].

Microscopic Instabilities

Although microscopic (local) buckling modes may alter the initial periodicity of the solid, they can be still detected by studying the response of a single unit cell and investigating the propagation of small-amplitude waves with arbitrary wave vector $\check{\mathbf{k}}$ superimposed on the current state of deformation [25–27]. While a real angular frequency ω corresponds to a propagating wave, a complex ω identifies a perturbation exponentially growing with time. Therefore, the transition between a stable and an unstable configuration is detected when the frequency vanishes (i.e. $\omega = 0$) and the new periodicity of the solid introduced by instability can be easily obtained by the corresponding wave vector.

To detect the onset of microscopic instabilities, we first deform the primitive unit cell to a certain extent and then investigate the propagation of elastic waves with different wave vector

$$\check{\mathbf{k}} = \check{k}_1 \mathbf{b}_1 + \check{k}_2 \mathbf{b}_2, \tag{28}$$

$\check{k}_1$ and $\check{k}_2$ being two real numbers. For each wave vector $\check{\mathbf{k}}$, the angular frequency ω is determined by solving the frequency domain equation (12). In this analysis quasi-periodic boundary conditions are applied, so that

$$\mathbf{u}(\mathbf{x} + \check{\mathbf{r}}) = \mathbf{u}(\mathbf{x}) \exp(i\check{\mathbf{k}} \cdot \check{\mathbf{r}}), \tag{29}$$

$\check{\mathbf{r}}$ denoting the distance in the current configuration between each pair of nodes periodically located on the boundary. Since most commercial finite-element packages do not support the complex-valued displacements

introduced by (29), following Aberg and Gudmundson [**?**] we split any complex-valued spatial function $\phi(\mathbf{x})$ into a real and an imaginary part,

$$\phi(\mathbf{x}) = \phi(\mathbf{x})^{re} + i\phi(\mathbf{x})^{im}. \tag{30}$$

The problem is then solved using two identical finite-element meshes for the unit cell, one for the real part and the other for the imaginary part, coupled by

$$\mathbf{u}^{re}(\mathbf{x}+\check{\mathbf{r}}) = \mathbf{u}^{re}(\mathbf{x})\cos(\check{\mathbf{k}}\cdot\check{\mathbf{r}}) - \mathbf{u}^{im}(\mathbf{x})\sin(\check{\mathbf{k}}\cdot\check{\mathbf{r}}), \tag{31}$$

$$\mathbf{u}^{im}(\mathbf{x}+\check{\mathbf{r}}) = \mathbf{u}^{re}(\mathbf{x})\sin(\check{\mathbf{k}}\cdot\check{\mathbf{r}}) + \mathbf{u}^{im}(\mathbf{x})\cos(\check{\mathbf{k}}\cdot\check{\mathbf{r}}). \tag{32}$$

A microscopic instability is detected at the first point along the loading path for which a wave vector $\check{\mathbf{k}}_{cr} = \check{k}_{1,cr}\mathbf{b}_1 + \check{k}_{2,cr}\mathbf{b}_2$ exist such that the corresponding angular frequency ω is zero. The instability will result in an enlarged unit cell with $n_1 \times n_2$ primitive unit cells, where

$$n_1 = \frac{1}{\check{k}_{1,cr}}, \quad \text{and} \quad n_2 = \frac{1}{\check{k}_{2,cr}}. \tag{33}$$

Macroscopic Instabilities

Following Geymonat et al. [25], we examine macroscopic instabilities by detecting loss of strong ellipticity of the overall response of the periodic structure. Specifically, macroscopic instabilities may develop whenever the condition

$$(\mathbf{m}\otimes\mathbf{M}) : \left[\mathbb{L}^H : (\mathbf{m}\otimes\mathbf{M})\right] > 0 \ , \quad \text{for all} \quad \mathbf{m}\otimes\mathbf{M} \neq \mathbf{0} \tag{34}$$

is first violated along the loading path, $\mathbb{L}^H$ denoting the homogenized incremental modulus.

Operationally, after determining the principal solution, the components of $\mathbb{L}^H$ are identified by subjecting the unit cells to four independent linear perturbations of the macroscopic deformation gradient [27]. Then loss of ellipticity is examined by checking condition (34) at every $\pi/360$ radian increment.

Post-buckling Analysis

As the second step, the post-buckling analysis is performed to capture the response of the structure beyond instability. Models with $n_1 \times n_2$ primitive unit cells are built, where n_1 and n_2 are determined in the buckling analysis. We first introduce a small random imperfection in the initial geometry by perturbing the position of each node. Here, we use a uniform random perturbation on each node with amplitude equal to one percent of the smallest element edge in the mesh.

Periodic boundary conditions are then applied, so that the positions of each pair of nodes periodically located on the boundary satisfy

$$\mathbf{x}(\mathbf{x}_0 + \mathbf{r_0}) - \mathbf{x}(\mathbf{x}_0) = \overline{\mathbf{F}}\cdot\mathbf{r_0} \tag{35}$$

where $\bar{\mathbf{F}}$ denotes the macroscopic deformation gradient and $\mathbf{r_0}$ the distance in the undeformed configuration between each pair of periodically located nodes.

Wave Propagation Analysis

In order to obtain the dispersion relation and evaluate the directionality of the propagating waves for the phononic crystals, frequency domain wave propagation analysis are performed on the deformed configurations generated by the post-buckling analysis. Bloch-type boundary conditions (eqns. (31) and (32)) are applied with the propagating bloch-wave vector $\mathbf{k}$ and updated spatial periodicity $\mathbf{r}$, so that

$$\mathbf{u}^{re}(\mathbf{x}+\mathbf{r}) = \mathbf{u}^{re}(\mathbf{x})\cos(\mathbf{k}\cdot\mathbf{r}) - \mathbf{u}^{im}(\mathbf{x})\sin(\mathbf{k}\cdot\mathbf{r}), \tag{36}$$

$$\mathbf{u}^{im}(\mathbf{x}+\mathbf{r}) = \mathbf{u}^{re}(\mathbf{x})\sin(\mathbf{k}\cdot\mathbf{r}) + \mathbf{u}^{im}(\mathbf{x})\cos(\mathbf{k}\cdot\mathbf{r}). \tag{37}$$

Focusing on the propagation of small-amplitude waves, we solve eqn. (12) using a perturbation method to obtain the dispersion relations $\omega = \omega(\mathbf{k})$.

For a 2D infinite periodic structure with spatial periodicity defined by (13) and (14), the periodicity in the reciprocal $\mathbf{k}$-space of the dispersion relation is given by [**?**]:

$$\omega(\mathbf{k}+\mathbf{g}) = \omega(\mathbf{k}), \tag{38}$$

with $\mathbf{g}$ defined in (17). Hence, due to translational symmetry specified by (38), we only need to study $\omega(\mathbf{k})$ for $\mathbf{k}$ vectors in the *first Brillouin zone* [**?**]. Moreover, the domain can be further reduced by taking advantage of rotational, reflectional and inversional symmetries of the first Brillouin zone. This allows us to define the *irreducible Brillouin zone* (IBZ) (see yellow triangle in Fig. 1) [19].

The phononic bandgaps are identified by checking all eigen-frequencies $\omega(\mathbf{k})$ for $\mathbf{k}$ vectors on the perimeter of the IBZ. The bandgaps (i.e. range in frequencies for which the propagation of waves is barred) are given by the frequency ranges within which no $\omega(\mathbf{k})$ exist. Numerically, a discrete set of $\mathbf{k}$ vectors on the IBZ perimeter need to be chosen in the band-gap calculation. For the simulations presented in this paper, twenty uniformly spaced points on each edge of the IBZ are used for the purpose of identifying band-gaps.

For the propagation directionality of the elastic wave in passing band of the phononic crystal, we investigate

the eigen-frequency surfaces over the entire IBZ to get the iso-frequency plots of the first two modes of the lowest passing bands: mode 1 being a shear-dominated mode and mode 2 representing a pressure-dominated mode. The phase velocity $\mathbf{v}_p$ and group velocity $\mathbf{v}_g$ of the propagating wave are then calculated as

$$\mathbf{v}_p = \frac{\omega \mathbf{k}}{\parallel \mathbf{k} \parallel^2} \ , \quad \mathbf{v}_g = \frac{\partial \omega}{\partial \mathbf{k}}. \tag{39}$$

Numerically, a discrete set of $\mathbf{k}$ vectors in the IBZ need to be chosen in the analysis. For the simulations presented in this paper, the results from four hundred uniformly distributed points inside the IBZ are used to interpolate the dispersion surface in $k-$space. Then, the value of dimensionless frequency $\tilde{f} = \omega a/(2\pi c_T) = 0.05$ is fixed for the calculation of the wave velocities of the low frequency modes (the first and second modes). Lastly, a standard central difference scheme is adopted for the calculation of the group velocity.

ADDITIONAL RESULTS FOR LOW-FREQUENCY DIRECTIONALITY

The results included in the main text suggest that *material nonlinearity* only affects the band gap and does not affect the propagation direction at low frequencies. Although in the main text we only include results for a square array of circular holes, we observed the same behavior also for different lattice patterns, non-linear material models and void volume fractions. Here, we report the results obtained not only for a square (Fig. 3), but also for triangular (Fig. 4) and trihexagonal (Fig. 5) arrays of circular holes with 60% initial porosity. The details and deformation configurations of these patterns can be found in [**?**]. In the figures, iso-frequency plots of the first shear-dominated (Mode 1) and pressure-dominated (Mode 2) modes are reported for the undeformed (top) and deformed (center and bottom) configurations. Moreover, for the deformed configurations both the Neo-Hookean model (i.e. Gent material with $J_m = \infty$, center) and the Gent model with $J_m = 0.5$ (bottom) are considered. It is important to note that for the deformed configurations the iso-frequency profiles obtained for phononic crystals made of Gent material with $J_m = \infty$ and 0.5 are found to be the same for all patterns. In contrast, we find a significant difference in the iso-frequency profiles between the undeformed and deformed configurations. These results suggest that only changes in geometry can be effectively used to tune the directional characteristics of the lowest two modes. This is due to the fact that the wavelength of the low frequency propagating modes are very long compared with the length scale of the local variations of stress field.

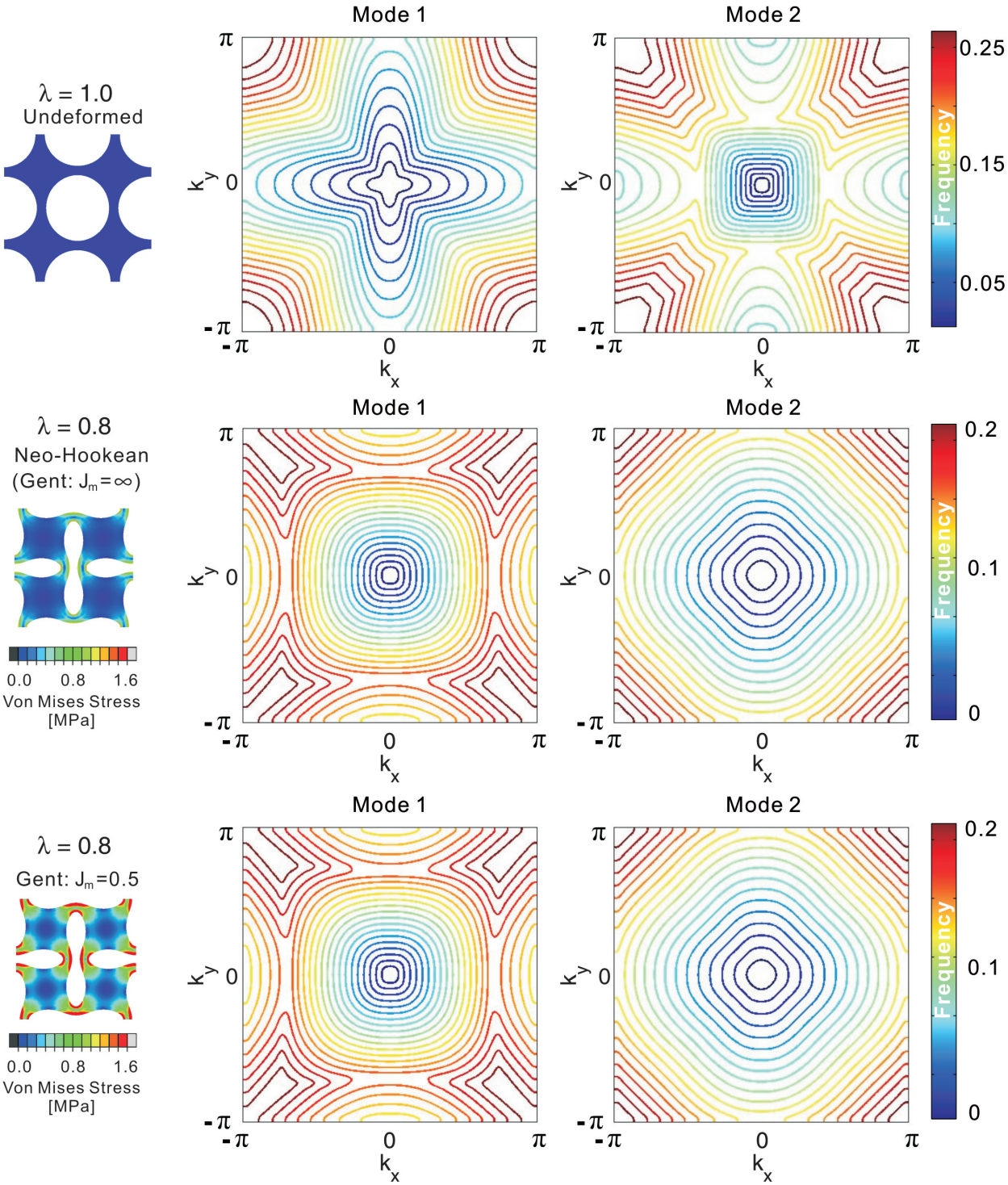

FIG. 3: Iso-frequency plots of the first two modes for the square lattice of circular voids. The results are reported in terms of the normalized frequency $\tilde{f} = \omega a/(2\pi c_T)$

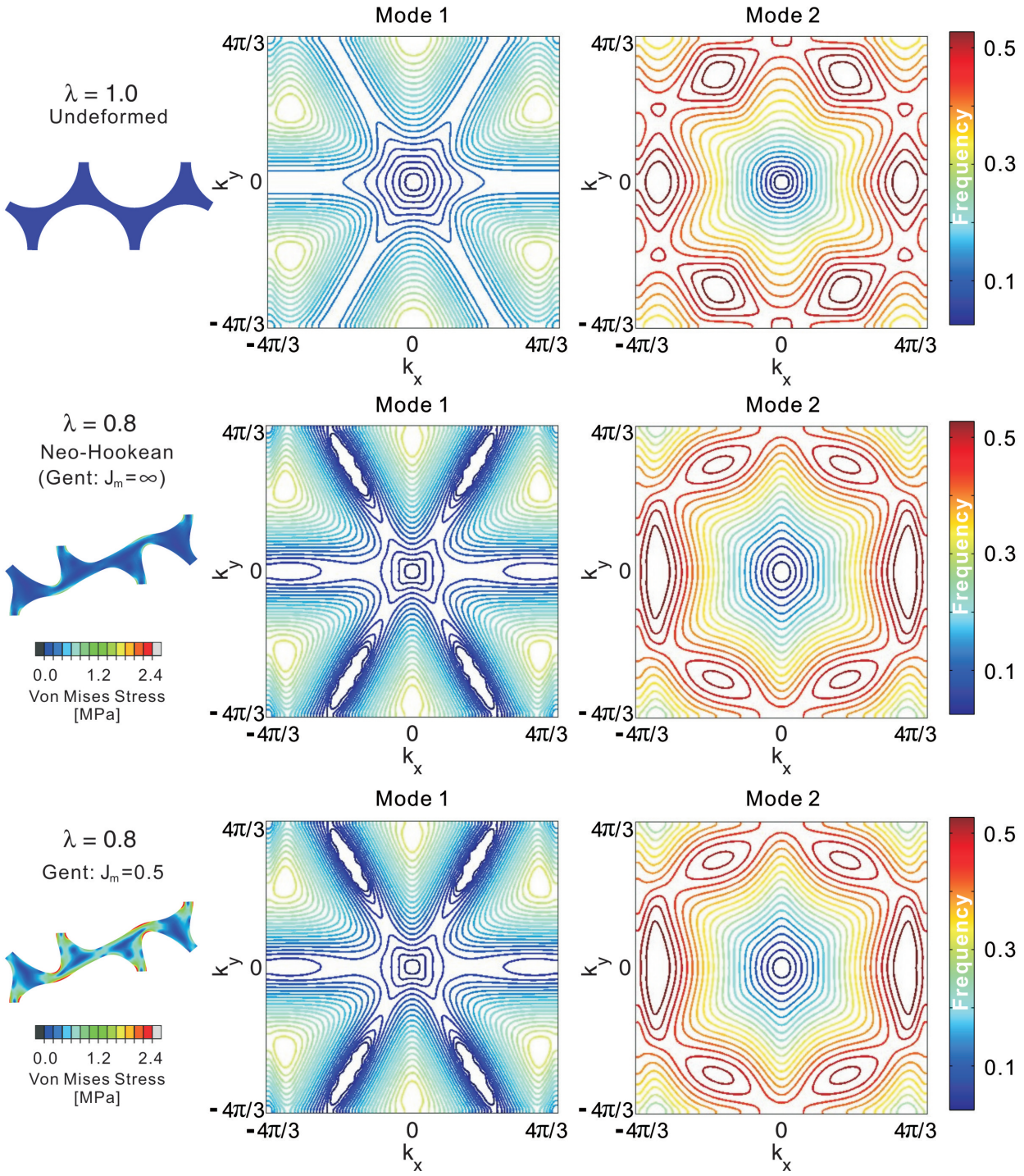

FIG. 4: Iso-frequency plots of the first two modes for the triangular lattice of circular voids. The results are reported in terms of the normalized frequency $\tilde{f} = \omega a/(2\pi c_T)$

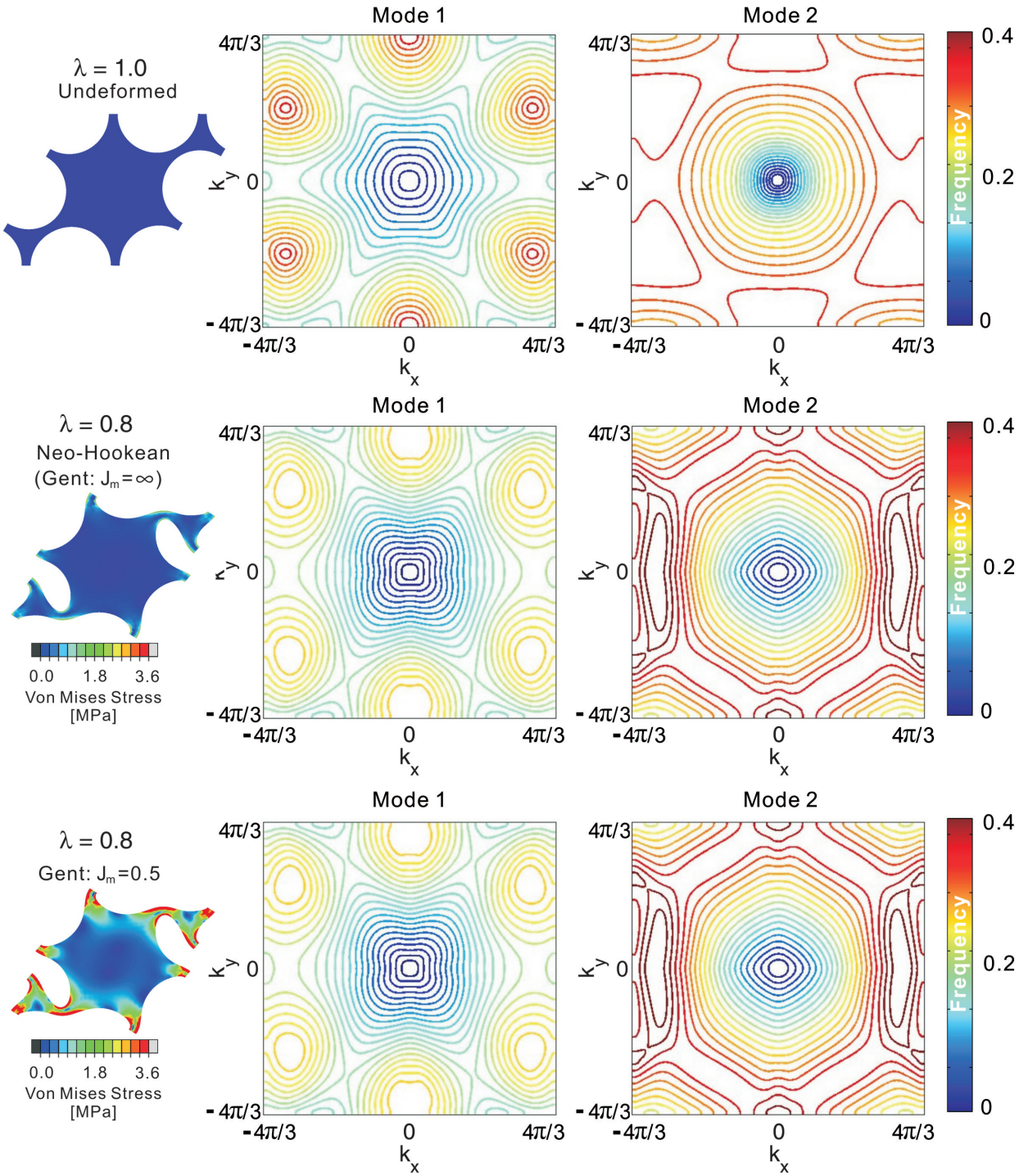

FIG. 5: Iso-frequency plots of the first two modes for the trihexagonal lattice of circular voids. The results are reported in terms of the normalized frequency $\tilde{f} = \omega a/(2\pi c_T)$

[1] M. Sigalas and E. Economou, Solid State Communications **86**, 141 (1993).

[2] M. S. Kushwaha, P. Halevi, L. Dobrzynski, and B. Djafari-Rouhani, Phys. Rev. Lett. **71**, 2022 (1993).

[3] M. Ruzzene and F. Scarpa, Phys. Sta. Sol. B **242**, 665 (2005).

[4] M. Maldovan and E. Thomas, Applied Physics B **83**, 595 (2006).

[5] K. Bertoldi and M. C. Boyce, Phys. Rev. B **78**, 184107 (2008).

[6] J. O. Vasseur, A. Hennion, B. Rouhani, F. Duval, B. Dubus, and Y. Pennec, J. App. Phys. **101**, 114904 (2007).

[7] W. Cheng, J. J. Wang, U. Jonas, G. Fytas, and N. Stefanou, Nat. Mater. **5**, 830 (2006).

[8] F. Casadei, L. Dozio, M. Ruzzene, and K. Cunefare, J. Sound. Vib. **329**, 3632 (2010).

[9] F. Casadei, B. Beck, K. A. Cunefare, and M. Ruzzene, Int. J. Solids Struc. **23**, 1169 (2012).

[10] M. Ruzzene, F. Scarpa, and F. Soranna, Smart. Mater. Struct. **12**, 363 (2003).

[11] M. Collet, M. Ouisse, M. Ruzzene, and M. N. Ichchou, Int. J. Sol. Struct. **48**, 2837 (2011).

[12] F. Casadei and J. Rimoli, International Journal of Solids and Structures (2013).

[13] E. Nolde, R. Craster, and J. Kaplunov, Journal of the Mechanics and Physics of Solids **59**, 651 (2011).

[14] S. Gonella and M. Ruzzene, International Journal of Solids and Structures **45**, 2897 (2008).

[15] S. Gonella and M. Ruzzene, Journal of Sound and Vibration **312**, 125 (2008).

[16] Vasseur, J. Phys. Condesed Mat. (1994).

[17] Zhou, J. App. Phys. (2009).

[18] Movchan, Mat. Sci. Eng. (2006).

[19] M. Maldovan and E. Thomas, *Periodic Materials and Interference Lithography for Photonics, Phononics and Mechanics* (Wiley-VCH, 2009).

[20] J. Jang, C. Koh, K. Bertoldi, M. Boyce, and E. Thomas, Nano Letters **9**, 2113 (2009).

[21] L. Wang and K. Bertoldi, International Journal of Solids and Structures **49**, 2881 (2012).

[22] See Supplementary Material at [URL] for the details of the general formulation and numerical procedures.

[23] A. Gent, Rubber Chem. Tech. **69**, 59 (1996).

[24] L. Treloar, Trans. Faraday Soc. **40**, 59 (1944).

[25] G. Geymonat, S. Muller, and N. Triantafyllidis, Arch. Ration. Mech. Anal. **122**, 231 (1993).

[26] N. Triantafyllidis, M. D. Nestorovic, and M. W. Schraad, J. Appl. Mech. **73**, 505 (2006).

[27] K. Bertoldi, M. Boyce, S. Deschanel, S. M. Prange, and T. Mullin., J. Mech. Phys. Solids **56**, 2642 (2008).

[28] Overvelde, S. Shan, and K. Bertoldi, Adv. Mater. **24**, 2337 (2012).